MIMO Active Vibration Control of Magnetically Suspended Flywheels for Satellite IPAC Service

Junyoung Park

Alan Palazzolo
Professor

Vibration Control and Electromechanical Laboratory,
Department of Mechanical Engineering,
MS 3123,
Texas A&M University,
College Station, TX 77843-3123

Raymond Beach
Power Technology Division,
NASA Glenn,
Cleveland, OH 44135

Theory and simulation results have demonstrated that four, variable speed flywheels could potentially provide the energy storage and attitude control functions of existing batteries and control moment gyros on a satellite. Past modeling and control algorithms were based on the assumption of rigidity in the flywheel's bearings and the satellite structure. This paper provides simulation results and theory, which eliminates this assumption utilizing control algorithms for active vibration control (AVC), flywheel shaft levitation, and integrated power transfer and attitude control (IPAC), that are effective even with low stiffness active magnetic bearings (AMBs) and flexible satellite appendages. The flywheel AVC and levitation tasks are provided by a multiple input–multiple output control law that enhances stability by reducing the dependence of the forward and backward gyroscopic poles with changes in flywheel speed. The control law is shown to be effective even for (1) large polar to transverse inertia ratios, which increases the stored energy density while causing the poles to become more speed dependent, and for (2) low bandwidth controllers shaped to suppress high frequency noise. Passive vibration dampers are designed to reduce the vibrations of flexible appendages of the satellite. Notch, low-pass, and bandpass filters are implemented in the AMB system to reduce and cancel high frequency, dynamic bearing forces and motor torques due to flywheel mass imbalance. Successful IPAC simulation results are presented with a 12% initial attitude error, large polar to transverse inertia ratio (I_P/I_T), structural flexibility, and unbalance mass disturbance. [DOI: 10.1115/1.2936846]

Introduction

Satellite weight and cost reduction goals may benefit from satellite integrated power and attitude control (IPAC). This will be accomplished by replacing the present energy storage system (electrochemical batteries) and attitude control torque actuator (control moment gyros) with an array of four high performance flywheels [1]. Successful implementation of IPAC requires a control approach that uncouples the attitude control and power transfer functions so as to avoid unplanned motion actuation due to power transfer and unplanned power transfer due to satellite motion actuation. This separation of functions is realized by utilizing attitude control torques obtained from the range space and power transfer torques from the orthogonal null space [1,2]. The prior IPAC literature focused on control algorithm development, which assumed that the satellite structure, flywheel shafts, and flywheel bearings were all rigid and that the flywheels were perfectly mass balanced to ignore the mass imbalance sinusoidal disturbance, which occurs at the spin speeds of the flywheels. This approach further simplified the problem by assuming that the motions of each flywheel could be adequately modeled with a single degree of freedom (DOF) per flywheel. The high speed, longevity, contamination, and loss requirements for these flywheels mandate that magnetic bearings (MBs) be utilized for suspension of the spinning rotor. The stiffness and damping of the MBs may be conveniently adjusted through gain changes in their feedback control electronics. In contrast to the assumptions employed in prior IPAC publications, the bearing stiffness is intentionally set at a low value to yield high frequency force isolation between the satellite and the spinning shafts. The versatility and low loss benefits of the MBs are gained only by incorporating sophisticated control algorithms to reject shaft and satellite borne disturbances while maintaining stable control. The MB control task is made complicated by the presence of speed dependent poles that result from gyroscopic moments of the spinning, vibrating shafts. The effect of speed dependent poles is magnified as an increased energy density demand on the flywheel is met by increasing the ratio (I_P/I_T) of the polar to transverse mass moments of inertia of the spinning rotors. These poles typically bifurcate from their zero speed values into a forward and a backward whirling pole pair, where the direction of vibration whirl is forward (backward) for whirl in the direction (opposite) of spin.

The rigid body gyroscopic poles asymptotically approach 0 Hz (backward pole) and (I_P/I_T) times spin frequency (forward pole) producing a very low frequency pole and a very high frequency pole for $I_P/I_T > 1$. This complicates the control task since increased active damping (derivative gain) is ineffective at low frequencies and causes noise amplification at high frequency. Effective MB control then requires a shift in strategy from providing phase lead by derivative gain changes to canceling gyroscopic torques utilizing a multiple input–multiple output (MIMO) control approach. The gyrotorque cancellation strategy requires that control "pitch" torques be applied to the rotor in one plane that are proportional to the shaft "yaw" angular motions in the quadrature plane. Hence, the shaft motions that are sensed near the MBs are converted, into coordinates that approximately describe the translation of the shaft's mass center and rigid body rotations about it, i.e., "CG" coordinates. These form the inputs to the MIMO control algorithm. The outputs of the control algorithm are CG force and torque commands that are converted to force commands at the MBs in both planes. The relationship between CG and MB coor-

Contributed by the Dynamic Systems, Measurement, and Control Division of ASME for publication in the JOURNAL OF DYNAMIC SYSTEMS, MEASUREMENT, AND CONTROL. Manuscript received January 9, 2007; final manuscript received December 20, 2007; published online June 5, 2008. Assoc. Editor: Mark Costello.

Copyright © 2008 by ASME

Downloaded From: http://asmedigitalcollection.asme.org/ on 04/07/2015 Terms of Use: http://asme.org/terms

dinates is presented in the Appendix. From this discussion, it is apparent that significant technical detail, as presented in this paper, is required to apply the general algorithms for IPAC that appear in literature to actual satellite systems.

The demand of maintaining a jitter free environment on the spacecraft inspired a novel contribution for utilizing bandpass filters that track rpm to assist in canceling shaking forces caused by the spinning flywheel shafts at their spin frequencies. The source of this force is that all MBs possess a passive negative stiffness making them open-loop unstable. The orbit (vibration) motion of the shaft section in the MB combines with the negative stiffness to produce a shaking force on the satellite at the shaft spin frequency. The tracked vibration component is inverted and routed through a gain stage to produce a signal for nulling the negative stiffness induced shaking forces.

The flexible appendage models in this paper are utilized to introduce low frequency modes into the plant as suggested to the authors by satellite design engineers. These may represent solar panels or other mission related equipment. For the sake of simplicity, the appendages are modeled as uniform beams with very low values of equivalent Young's modulus to produce low frequency and lightly damped modes. Vibrations of the appendages during an attitude maneuver cause low frequency, small amplitude oscillations in the power transferred into or out of the flywheel array. These vibrations and the ensuing oscillations are significantly attenuated by attachment of a "vibration control mass (VCM)" at the free end of both appendages. The optimal stiffness and damping of the VCM are obtained with a simplified assumed mode model of the appendages. The following sections attempt to answer questions posed by satellite design engineers related to implementing IPAC: (a) Is satellite IPAC effective with structural flexibility included in the bearings and appendages, (b) is it possible to stabilize all eigenvalues related to the flywheel-MB system in the IPAC system of (a), and (c) can low frequency appendage mode interference of IPACS be passively suppressed.

Literature Review

Utilizing flywheels for energy storage on satellites was suggested as early as 1961 in the Roes paper [3]. Sindlinger [4] and Brunet [5] discussed the advantages of the MB suspension of a flywheel for attitude control and energy storage. Flatley [6] employed a tetrahedral array of four momentum wheels to consider the issues associated with applying wheel control torques for simultaneous attitude control and energy storage. Tsiotras [7] introduced a logarithmic term for a kinematical parameter in the Lyapunov function that makes the controller corresponding to this parameter become linear. Schaub et al. [8] presented a nonlinear feedforward/feedback controller for a prototype, landmark-tracking spacecraft. Near-minimum time and near-minimum fuel reference control torques were utilized in this paper. Tsiotras et al. [1] presented a control law for an IPAC system for a rigid satellite with momentum wheels/reaction wheels. Kim [2] outlined implementation of IPAC for a rigid structural satellite with SISO MB control system. Okada et al. [9] utilized a proportional, cross-feedback control to stabilize a high-speed rotor supported on MBs. Ahrens et al. [10] also verified that the cross-feedback control leads to better system performance and improved stability for a flywheel-AMB energy storage system with strong gyroscopic coupling moments. Na [11] presented algorithms for fault-tolerant control of heteropolar MBs. Herzog et al. [12] proposed a generalized narrow-band notch filter, which is inserted into the multivariable feedback without destabilizing the closed loop and has advantages in terms of runtime complexity and analytical verification of closed-loop stability. Bhat and Bernstein [13] showed that a continuous dynamical system on a state space that has the structure of a vector bundle on a compact manifold possesses no globally asymptotically stable equilibrium and they explained how attitude stabilizing controllers appearing in literature lead to unwinding instead of global asymptotic stability. Parman and Koguchi [14] presented a three-dimensional rest-to-rest attitude control of a flexible spacecraft equipped with on-off reaction jets, utilizing finite elements for modeling of flexible solar panels and with a Lagrangian formulation for the equations of motion. They applied time-optimal and fuel-efficient input shapers to reduce the residual oscillation of its motion at several natural frequencies in order to get an expected pointing precision of the satellite. MB supported flywheels for energy storage and satellite attitude systems [2,15–19] appear in many publications, but without reference to MIMO (Gyro) control for higher polar to transverse inertia ratio stability or to utilization of bandpass filters for removing transmitted forces induced by the MB position stiffness. NASA related flywheel R&D includes the pioneering work of Kirk et al. [20–23] for improving energy density and for incorporating MBs. The work of Kenny et al. [24] integrated sensorless field oriented motor control, which was successfully demonstrated at 60,000 rpm on a NASA flywheel. Christopher and Beach provide a comprehensive overview of the NASA Glenn flywheel program in Ref. [25]. The present paper demonstrates the effectiveness of a cross coupled, MIMO AMB control approach for providing rotordynamic stability and vibration suppression during a simulated IPAC maneuver with flywheel bearing and satellite flexibility included in the model. The term cross coupled control signifies application of control torques in one plane, i.e., x-y, due to angular motion in the quadrature plane, i.e., x-z. This mimics the action of a gyroscopic torque, which acts in one plane and is proportional to the angular velocity in the quadrature plane. The MIMO control implements a strategy of gyroscopic torque cancellation, which reduces the dependence of the forward and backward conical mode poles on spin speed. This simplifies the control law by reducing its dependence on spin speed and reduces high frequency noise amplification by lowering the frequency of the forward conical mode and, in turn, lowering the level of required derivative gain.

Theory and Analysis

Structural Dynamics. The motions in the IPAC satellite model (Fig. 1) are described with the following coordinate systems:

(a) an inertially fixed coordinate system for the satellite's center of mass translations: $(\hat{n}_1,\hat{n}_2,\hat{n}_3)$
(b) four satellite flywheel housing coordinates to indicate the very small relative motions of the flywheels with respect to the satellite at their housing (stator) locations: $(\hat{h}_{f,1},\hat{h}_{f,2},\hat{h}_{f,3})$
(c) satellite body fixed coordinates for defining the satellite's angular velocity components: $(\hat{s}_1,\hat{s}_2,\hat{s}_3)$
(d) four coordinate frames that precess, but do not spin, with the axisymmetric flywheels. The flywheel inertias are constant in these frames; thus, the frames require only two instead of three angular coordinates to define the direction cosine matrix for each flywheel: $(\hat{f}_1,\hat{f}_2,\hat{f}_3)$
(e) two satellite fixed coordinate frames are oriented along the undeformed appendages. Relative motion coordinates $(\hat{a}_1,\hat{a}_2,\hat{a}_3)$ define the small deflections of the appendages with respect to these coordinate axes: $(\hat{h}_{a,1},\hat{h}_{a,2},\hat{h}_{a,3})$

Only (a) and (c) coordinate systems are shown in Fig. 1 due to complexity. The rest of coordinate systems are depicted in Figs. 15 and 16.

Translational Motions of a Rigid Flywheel and Flexible Appendage Models. The translational motion for one rigid flywheel module is obtained from the coordinate configuration shown in Fig. 2. Based on this, the translational motion of flywheel in the

Downloaded From: http://asmedigitalcollection.asme.org/ on 04/07/2015 Terms of Use: http://asme.org/terms

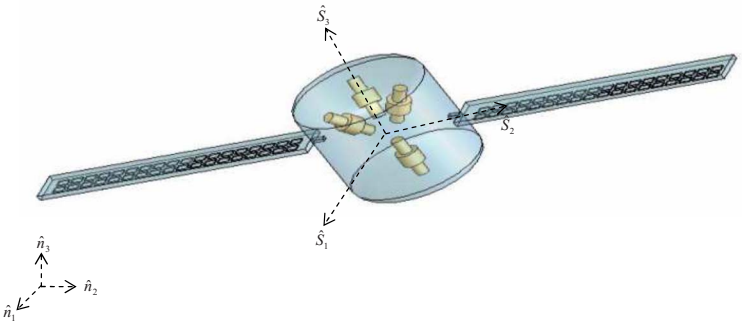

Fig. 1 System model including the satellite body, flexible appendages, and four flywheel arrays

flywheel housing frame can be expressed in Eqs. (5) and (6). The flexible appendage model is represented as a series of nonspinning, rigid disks (inertia stations) interconnected with flexible, massless beam elements, which follows the standard lumped mass approach commonly employed with finite element models. The rigid disks are modeled as executing general 3D motion even though their motions with respect to an observer attached to the satellite are very small. The 12 DOFs at the end nodes of the beam element are illustrated in Fig. 3.

The nodal rotational and translational DOFs of the two-noded, six DOF per node beam element in Fig. 3 are arranged in the element displacement vector with the following convention:

$$\mathbf{U}_e = [x_i \quad y_i \quad z_i \quad \theta_{xi} \quad \theta_{yi} \quad \theta_{zi} \quad x_{i+1} \quad y_{i+1} \quad z_{i+1} \quad \theta_{x,i+1} \quad \theta_{y,i+1} \quad \theta_{z,i+1}]^T \tag{1}$$

The diagonal lumped mass matrix and stiffness matrix for the beam element are given in Eqs. (2) and (3). It is important to note that Eq. (2) is shown only to identify the inertia associated with each DOF. The mass matrix in Eq. (2) is not multiplied times the second time derivative of Eq. (1) to obtain inertia forces, which are instead obtained via the full 3D nonlinear Euler equations. A proportional damping matrix is employed to account for the damping inherent in the material.

$$\mathbf{M}_e = \mathrm{diag}([m_i \quad m_i \quad m_i \quad I_{p,i} \quad I_{t,i} \quad I_{t,i} \quad m_{i+1} \quad m_{i+1} \quad m_{i+1} \quad I_{p,i+1} \quad I_{t,i+1} \quad I_{t,i+1}]) \tag{2}$$

$$\mathbf{K}_e = \begin{bmatrix} a_1^e & 0 & 0 & 0 & 0 & 0 & -a_1^e & 0 & 0 & 0 & 0 & 0 \\ & a_2^e & 0 & 0 & 0 & a_3^e & 0 & -a_2^e & 0 & 0 & 0 & a_3^e \\ & & a_4^e & 0 & a_5^e & 0 & 0 & 0 & -a_4^e & 0 & a_5^e & 0 \\ & S & & a_6^e & 0 & 0 & 0 & 0 & 0 & -a_6^e & 0 & 0 \\ & & Y & & a_7^e & 0 & 0 & 0 & -a_5^e & 0 & a_8^e & 0 \\ & & & M & & a_9^e & 0 & -a_3^e & 0 & 0 & 0 & a_{10}^e \\ & & & & M & & a_1^e & 0 & 0 & 0 & 0 & 0 \\ & & & & & E & & a_2^e & 0 & 0 & 0 & -a_3^e \\ & & & & & & T & & a_4^e & 0 & -a_5^e & 0 \\ & & & & & & & R & & a_6^e & 0 & 0 \\ & & & & & & & & I & & a_7^e & 0 \\ & & & & & & & & & C & & a_9^e \end{bmatrix} \tag{3}$$

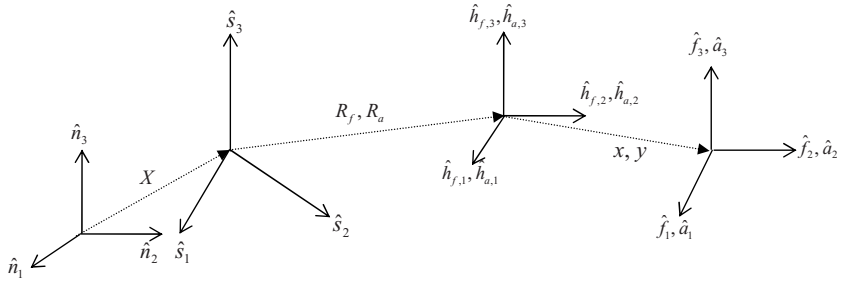

$\hat{n}_i, i=1,2,3$: **Inertial reference coordinates** $\quad \hat{h}_{f,i}, i=1,2,3$: **Flywheel housing coordinates**

$\hat{s}_i, i=1,2,3$: **Satellite body fixed coordinates** $\quad \hat{h}_{a,i}, i=1,2,3$: **Appendage reference coordinates**

$\hat{f}_i, i=1,2,3$: **Flywheel non-spinning body coordinates** $\quad \hat{a}_i, i=1,2,3$: **Appendage body coordinates**

Fig. 2 Inertial, satellite, housing, flywheel, and appendage coordinate systems

Downloaded From: http://asmedigitalcollection.asme.org/ on 04/07/2015 Terms of Use: http://asme.org/terms

$$C_e = \left(\frac{2\xi}{\omega}\right) K_e \tag{4}$$

where

$$a_1^e = E^e A^e / L_e, \quad a_2^e = 12E^e I_{x3}^e / L_e^3,$$

$$a_3^e = 6E^e I_{x3}^e / L_e^2, \quad a_4^e = 12E^e I_{x2}^e / L_e^3 \quad a_5^e = -6E^e I_{x2}^e / L_e^2$$

$$a_6^e = G^e J^e / L_e, \quad a_7^e = 4E^e I_{x2}^e / L_e, \quad a_8^e = 2E^e I_{x2}^e / L_e$$

$$a_9^e = 4E^e I_{x3}^e / L_e, \quad a_{10}^e = 2E^e I_{x3}^e / L_e$$

The equations of motion for the flexible appendages are of the same form as for the flywheels except that the spin terms are set to zero.

Translational Equation of Motion for a Rigid Flywheel Model. From Fig. 2,

$$m_f \ddot{X}_{f/n}^h = F_f \tag{5}$$

$$m_f\{(\ddot{x})_h + [h_f n]\ddot{X} - X_{f/s}^h \times [h_f s]\dot{\Omega}_s\} = F_f - 2m_f \times [h_f s]\Omega_s \times (\dot{x})_h - m_f\{[h_f s]\Omega_s \times ([h_f s]\Omega_s \times X_{f/s}^h)\} \tag{6}$$

Translational Equations of Motion for a Pair of Neighboring Rigid Disks in the Flexible Appendage Model.

ith Disk Translational Motion

$$m_{i,a}\{(\ddot{y}_i)_h + [h_a n]_i \ddot{X}_i - X_{ia/s}^h \times [h_a s]_i \dot{\Omega}_{i,s}\} + F_{i,c} + F_{i,s} = F_{i,a} - 2m_{i,a}[h_a s]_i \Omega_{i,s} \times (\dot{y}_i)_h - m_{i,a}\{[h_a s]_i \Omega_{i,s} \times ([h_a s]_i \Omega_{i,s} \times X_{ia/s}^h)\} \tag{7}$$

$i+1th$ Disk Translational Motion

$$m_{i+1,a}\{(\ddot{y}_{i+1})_h + [h_a n]_{i+1} X_{i+1} - X_{i+1a/s}^h \times [h_a s]_{i+1} \dot{\Omega}_{i+1,s}\} + F_{i+1,c} + F_{i+1,s} = F_{i+1,a} - 2m_{i+1,a}[h_a s]_{i+1} \Omega_{i+1,s} \times (\dot{y}_{i+1})_h - m_{i+1,a}\{[h_a s]_{i+1} \Omega_{i+1,s} \times ([h_a s]_{i+1} \Omega_{i+1,s} \times X_{i+1,a/s}^h)\} \tag{8}$$

where $x = x_1 \hat{h}_{f,1} + x_2 \hat{h}_{f,2} + x_3 \hat{h}_{f,3}$ is the displacement of flywheel relative to flywheel housing, $y = y_1 \hat{h}_{a,1} + y_2 \hat{h}_{a,2} + y_3 \hat{h}_{a,3}$ is the displacement of appendage relative to appendage reference frame, $R_f = R_{f,1}\hat{s}_1 + R_{f,2}\hat{s}_2 + R_{f,3}\hat{s}_3$ is the offset distance between flywheel housing mass center and satellite CG, $R_a = R_{a,1}\hat{s}_1 + R_{a,2}\hat{s}_2 + R_{a,3}\hat{s}_3$ is the offset distance between a point on the appendage reference and satellite CG, $X = X_1\hat{n}_1 + X_2\hat{n}_2 + X_3\hat{n}_3$ is the displacement of the satellite mass center relative to the inertial frame, $X_{f/s}^h = x + [h_f s]R_f$ is the displacement of flywheel mass center relative to the satellite in the flywheel housing frame, $\dot{X}_{f/s}^h = (\dot{x})_h + [h_f s]\Omega_s \times x + [h_f s](\Omega_s \times R_f)$ is the flywheel CG velocity relative to the satellite in the flywheel housing frame, and $\dot{X}_{f/n}^h = (\dot{x})_h + [h_f s]\Omega_s \times x + [h_f s](\Omega_s \times R_f) + [h_f n]\dot{X}$ is the flywheel CG velocity relative to the inertial frame in the flywheel housing frame.

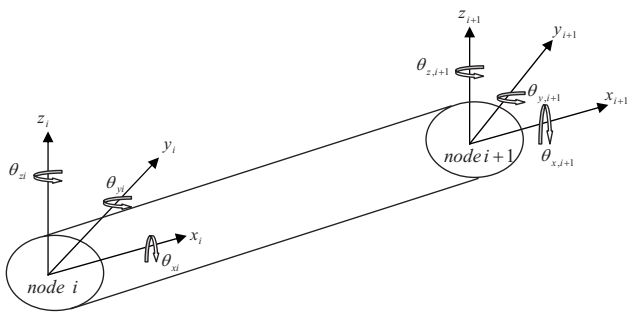

Fig. 3 Nodal DOFs for a 3D beam type finite element

Rotational Motion of a Rigid Flywheel and Flexible Appendage Models. The rotational equations of motion for a rigid flywheel model are derived in a nonspinning coordinate system. The flywheel angular momentum vector is given by Eq. (9) and the flywheel rotational equation of motion is obtained through differentiation of the angular momentum vector.

Rotational Equations of Motion for a Rigid Flywheel Model.

$$H_f = I_f \omega_f \quad \text{where } \omega_f = \Omega_f + [fs]\Omega_s \tag{9}$$

$$\dot{H}_f = \frac{d}{dt}(H_f)_f + \omega_{f/n} \times H_f = I_f \frac{d}{dt}(\Omega_f + [fs]\Omega_s)_f + \omega_{f/n} \times H_f = T_f \tag{10}$$

$$I_f \dot{\Omega}_f + I_f [fs]\dot{\Omega}_s = T_f - \tilde{\omega}_f I_f \Omega_f + (I_f \tilde{\Omega}_f - \tilde{\omega}_f I_f)[fs]\Omega_s \tag{11}$$

Rotational Equations of Motion for a Pair of Neighboring Rigid Disks in the Flexible Appendage Model. ith Disk Rotational Motion

$$I_{i,a}\dot{\Omega}_{i,a} + I_{i,a}[as]_i \dot{\Omega}_{i,s} + T_{i,c} + T_{i,s} = T_{i,a} - \tilde{\omega}_{i,a} I_{i,a} \Omega_{i,a} + (I_{i,a}\tilde{\Omega}_{i,a} - \tilde{\omega}_{i,a} I_{i,a})[as]_i \Omega_{i,s} \tag{12}$$

$i+1th$ Disk Rotational Motion

$$I_{i+1,a}\dot{\Omega}_{i+1,a} + I_{i+1,a}[as]_{i+1}\dot{\Omega}_{i+1,s} + T_{i+1,c} + T_{i+1,s} = T_{i+1,a} - \tilde{\omega}_{i+1,a} I_{i+1,a} \Omega_{i+1,a} + (I_{i+1,a}\tilde{\Omega}_{i+1,a} - \tilde{\omega}_{i+1,a} I_{i+1,a})[as]_{i+1}\Omega_{i+1,s} \tag{13}$$

where $T_f = T_{\text{mt}} + T_{\text{Mb}}$ is the torque applied to the flywheel.

$$F_{i,s} = K_{e,(1:3,1:12)} U_e, \quad F_{i+1,s} = K_{e,(7:9,1:12)} U_e$$

$$T_{i,s} = K_{e,(4:6,1:12)} U_e, \quad T_{i+1,s} = K_{e,(10:12,1:12)} U_e$$

$$F_{i,c} = C_{e,(1:3,1:12)} \dot{U}_e, \quad F_{i+1,c} = C_{e,(7:9,1:12)} \dot{U}_e$$

$$T_{i,c} = C_{e,(4:6,1:12)} \dot{U}_e, \quad T_{i+1,c} = C_{e,(10:12,1:12)} \dot{U}_e$$

Satellite Rotational and Translational Equations of Motions

Rotation (No External Torques).

$$I_s \dot{\Omega}_s + \tilde{\Omega}_s I_s \Omega_s = -\sum [fs]^T T_f - \sum \{\dot{X}_f^h \times m_f \dot{X}_f^h + X_f^h \times F_f\} - \sum \left[\sum_{j=1}^{m} [a_j s]^T T_{a,j} \right] - \sum \left[\sum_{j=1}^{m} \{(\dot{X}_{a,j/s}^{h,j}) \times m_{a,j}(\dot{X}_{a,j/n}^{h,j}) + (X_{a,j/s}^{h,j}) \times (F_{a,j})\} \right] \tag{14}$$

Translation (No External Forces).

$$M_s \ddot{X} = -\sum [hn]^T F_f - \sum \left[\sum_{j=1}^{m} [h_{a,j} n]^T F_{a,j} \right] \tag{15}$$

Reference Motion Design. Euler's principal axis (EPA) theorem shows that a rigid body may undergo an arbitrary three-dimensional reorientation by rotating about a single "principal" axis. A near-minimum-time control law for single axis, rest-to-rest maneuver of a rigid body has the form [26]

Downloaded From: http://asmedigitalcollection.asme.org/ on 04/07/2015 Terms of Use: http://asme.org/terms

$$I\ddot{\theta} = u = \pm u_{\max} f(\Delta t, t_f, t) \tag{16}$$

$$f(\Delta t, t_f, t) = \begin{cases} \left(\frac{t}{\Delta t}\right)^2 \left[3 - 2\left(\frac{t}{\Delta t}\right)\right] & \text{for } 0 \le t \le \Delta t \\ 1 & \text{for } \Delta t \le t \le \frac{t_f}{2} - \Delta t \equiv t_1 \\ 1 - 2\left(\frac{t - t_1}{2\Delta t}\right)^2 \left[3 - 2\left(\frac{t - t_1}{2\Delta t}\right)\right] & \text{for } t_1 \le t \le \frac{t_f}{2} + \Delta t \equiv t_2 \\ -1 & \text{for } t_2 \le t \le t_f - \Delta t \equiv t_3 \\ -1 + \left(\frac{t - t_3}{\Delta t}\right)^2 \left[3 - 2\left(\frac{t - t_3}{\Delta t}\right)\right] & \text{for } t_3 \le t \le t_f \end{cases} \tag{17}$$

Integration of Eq. (16) yields

$$\dot{\theta}(t) = \dot{\theta}_0 + \frac{u_{\max}}{I} \int_{t_0}^{t} f(\Delta t, t_f, \tau) d\tau \tag{18}$$

$$\theta(t) = \theta_0 + (t - t_0)\dot{\theta}_0 + \frac{u_{\max}}{I} \int_{t_0}^{t} \int_{t_0}^{\tau_1} f(\Delta t, t_f, \tau_2) d\tau_2 d\tau_1 \tag{19}$$

For rest-to-rest maneuver, we impose the boundary conditions At $t_0 = 0$,

$$\theta(0) = \theta_0 = 0, \quad \dot{\theta}(0) = \dot{\theta}_0 = 0 \tag{20}$$

At time t_f,

$$\theta(t_f) = \theta_f, \quad \dot{\theta}(t_f) = \dot{\theta}_f = 0 \tag{21}$$

and upon carrying out the integrations implies in Eqs. (18) and (19), we obtain the useful relationship

$$\theta_f = \frac{u_{\max}}{I} \left[\frac{1}{4} - \frac{1}{2}\alpha + \frac{1}{10}\alpha^2\right] t_f^2 \tag{22}$$

Let $\tilde{A} = u_{\max}/I$ in Eqs. (18) and (19). Plug Eq. (22) into $\tilde{A}$, then we obtain

$$\tilde{A} = \frac{4\theta_f}{(1 - 2\alpha + 0.4\alpha^2) t_f^2} \tag{23}$$

The above equations (Eqs. (16), (18), and (19)) can be expressed by

$$\ddot{\theta} = \tilde{A} f(\Delta t, t_f, t)$$

$$\dot{\theta}(t) = \tilde{A} \int_{t_0}^{t} f(\Delta t, t_f, \tau) d\tau \tag{24}$$

$$\theta(t) = \tilde{A} \int_{t_0}^{t} \int_{t_0}^{\tau_1} f(\Delta t, t_f, \tau_2) d\tau_2 d\tau_1$$

If EPA axis of rotation is determined as l, then the corresponding angular velocity, angular acceleration, and modified Rodrigues parameters (MRPs) are given by

$$\Omega_{sr}(t) = l\dot{\theta}(t), \quad \dot{\Omega}_{sr}(t) = l\ddot{\theta}(t) \text{ and } \sigma_{sr}(t) = l \tan\left(\frac{\theta(t)}{4}\right) \tag{25}$$

where $l = [l_1\ l_2\ l_3]^T$ is the Euler's principal axis. The satellite reference motions such as angular acceleration, angular velocity, and MRP $(\dot{\Omega}_{sr}, \Omega_{sr}, \sigma_{sr})$ can be obtained from Eqs. (16)–(25).

Flywheel Speed Control for IPAC. System control includes both position control for each of the magnetically supported flywheels and control of the flywheel speeds for actuation and power transfer in IPAC service. This section contains the analysis for the IPAC law, which consists of a nonlinear, state feedback, asymptotic stable [17], tracking control law derived with a Lyapunov approach [7].

IPAC Law. Consider the following candidate Lyapunov function [27,28] expressed in terms of the tracking error and its time derivative.

$$V = \tfrac{1}{2}\delta\omega^T I_s \delta\omega + 2k_2 \ln(1 + \delta\sigma^T \delta\sigma) \tag{26}$$

$$\dot{V} = \delta\omega^T I_s \delta\dot{\omega} + 4k_2 \frac{\delta\sigma^T \delta\dot{\sigma}}{1 + \delta\sigma^T \delta\sigma} = \delta\omega^T I_s \delta\dot{\omega} + 4k_2 \frac{\delta\sigma^T f(\delta\sigma)\delta\omega}{1 + \delta\sigma^T \delta\sigma}$$

$$= \delta\omega^T (I_s \delta\dot{\omega} + k_2 \delta\sigma) \tag{27}$$

where

$$\delta\dot{\sigma} = f(\delta\sigma)\delta\omega, \quad \delta\sigma^T f(\delta\sigma)\delta\omega = \frac{1 + \delta\sigma^T\delta\sigma}{4} \delta\sigma^T \delta\omega \text{ (Ref. 28)} \tag{28}$$

Let the term in the parentheses of Eq. (27) be equal to $-k_1\delta\omega$, then Eq. (27) yields

$$\dot{V} = -k_1 \delta\omega^T \delta\omega \le 0 \quad \text{for all } \delta\omega \text{ and } k_1 > 0, \quad \text{where } I_s\delta\dot{\omega} + k_2\delta\sigma = -k_1\delta\omega \tag{29}$$

The angular velocity error and its time derivative can be written as Eqs. (30) and (31) in the satellite coordinates

$$\delta\omega = \Omega_s - [sr]\Omega_{sr} \tag{30}$$

$$\delta\dot{\omega} = \dot{\Omega}_s - \left(\left(\frac{d}{dt}[sr]\right)\Omega_{sr} + [sr]\dot{\Omega}_{sr}\right)$$

$$= \dot{\Omega}_s - (-\tilde{\Omega}_s[sr]\Omega_{sr} + [sr]\dot{\Omega}_{sr})$$

$$= \dot{\Omega}_s - [sr]\dot{\Omega}_{sr} + (\Omega_s) \times (\Omega_s - \delta\omega)$$

$$= \dot{\Omega}_s - [sr]\dot{\Omega}_{sr} + \delta\tilde{\omega}\Omega_s \tag{31}$$

where

$$\frac{d}{dt}([sr]) = \frac{d}{dt}([sn][rn]^T) = \frac{d}{dt}([sn])[rn]^T + [sn]\frac{d}{dt}([rn]^T)$$

$$= -\tilde{\Omega}_s[sr] + [sr]\tilde{\Omega}_{sr}$$

The effective torque required for the actual motion is

$$\Gamma_s = I_s\dot{\Omega}_s + \tilde{\Omega}_s I_s \Omega_s \quad \text{or } \dot{\Omega}_s = I_s^{-1}(\Gamma_s - \tilde{\Omega}_s I_s \Omega_s) \tag{32}$$

Premultiply Eq. (31) by I_s to obtain Eq. (33) (error motion). Equation (34) is obtained by substituting Eq. (32) into Eq. (33),

Downloaded From: http://asmedigitalcollection.asme.org/ on 04/07/2015 Terms of Use: http://asme.org/terms

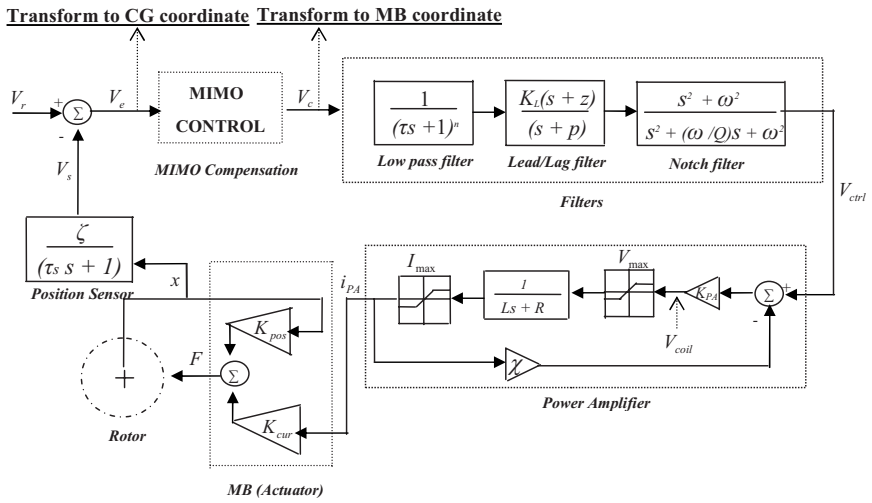

Fig. 4 MB suspension system feedback control diagram for MIMO (Gyro)

$$I_s\delta\dot{\omega} = I_s\dot{\Omega}_s - I_s[sr]\dot{\Omega}_{sr} + I_s\delta\tilde{\omega}\Omega_s \tag{33}$$

$$I_s\delta\dot{\omega} = \Gamma_s - \tilde{\Omega}_s I_s\Omega_s - I_s[sr]\dot{\Omega}_{sr} + I_s\delta\tilde{\omega}\Omega_s \tag{34}$$

Equating Eqs. (29) and (34) to obtain

$$I_s\delta\dot{\omega} = \Gamma_s - \tilde{\Omega}_s I_s\Omega_s - I_s[sr]\dot{\Omega}_{sr} + I_s\delta\tilde{\omega}\Omega_s = -k_1\delta\omega - k_2\delta\sigma \tag{35}$$

$$\Gamma_s = \tau_s - \sum [fs]^T T_{\mathrm{mt}} \tag{36}$$

then, the flywheel control motor torques are obtained by substituting Eq. (36) into Eq. (35),

$$\sum [fs]^T T_{\mathrm{mt}} = \tau_s - \tilde{\Omega}_s I_s\Omega_s - I_s[sr]\dot{\Omega}_{sr} + I_s\delta\tilde{\omega}\Omega_s + k_1\delta\omega + k_2\delta\sigma \tag{37}$$

$$\tau_s = -\sum [fs]^T T_{\mathrm{MB}} - \sum [hs]^T(\dot{X}_f^h \times m_f\dot{X}_f^h + X_f^h \times F_f) - \sum \left[\sum_{j=1}^{m} [a_j s]^T T_{a,j}\right]$$

where

$$-\sum \left[\sum_{j=1}^{m} [h_{a,j}s]^T(\dot{X}_{a,j/s}^h \times m_{a,j}\dot{X}_{a,j/n}^h + X_{a,j/s}^h \times F_{a,j})\right]$$

The Lyapunov function V is positive definite and radially unbounded in terms of the tracking errors. The time derivative of V given by Eq. (29) is negative definite. Therefore, the departure motion (34) and kinematical equation for the departure motion (28) with the feedback motor torque control law (37) are asymptotically stable.

Torque Distributions and Power Tracking. The individual flywheel motor torques and the torque required by the satellite for attitude control are related by

$$T_s = \mathbf{A}T_{\mathrm{mt}} \tag{38}$$

where T_{mt} and T_s are the required torques applied to the flywheel and satellite, respectively, and $\mathbf{A}$ is the $3\times n$ system configuration matrix (n is the number of flywheel) with columns equal to the unit vectors of the flywheel housing coordinate axes [1]. The solution of Eq. (38), T_{mt}, is a linear combination of vectors belongs to the range space of matrix $\mathbf{A}$. If the number of flywheel modules is less than 3, the system is overdetermined and a solution may not exist. If the number is 3, the solution is uniquely determined and if the number of flywheel modules exceeds 3, the system is underdetermined and there exists an infinite number of solutions. For this paper, the satellite has four flywheel modules, which form an underdetermined system. One useful solution is the minimum norm solution obtained by using a pseudoinverse. The general solution for T_{mt} is given by

$$T_{\mathrm{mt}} = \mathbf{A}^+\mathbf{T}_s + T_n \quad \text{where } \mathbf{A}^+ = A^T(AA^T)^{-1} \tag{39}$$

The vector $\mathbf{A}^+\mathbf{T}_s$ belongs to the range space of A^T and T_n belongs to the null space of A; in other words, $AT_n=0$, so T_n does not affect the satellite motion. Simultaneous attitude control and power tracking require that the torque satisfies the following set of linear equations:

$$\begin{pmatrix} A \\ \omega_f^T \end{pmatrix} T_{\mathrm{mt}} = \begin{pmatrix} T_s \\ P \end{pmatrix} \tag{40}$$

The second constraint of Eq. (40) is written as $\omega_f^T(\mathbf{A}^+\mathbf{T}_s + T_n) = P$.

Define the modified power as

$$P_m = P - \omega_f^T\mathbf{A}^+\mathbf{T}_s = \omega_f^T T_n \tag{41}$$

The power torque T_n belongs to the null space of the configuration matrix $\mathbf{A}$; therefore, there exists a vector $\boldsymbol{\eta}$ in the null space, which satisfies

$$T_n = \mathbf{P}_n\boldsymbol{\eta} \tag{42}$$

where $\mathbf{P}_n = I_{n\times n} - A^T(AA^T)^{-1}A$ is the orthogonal projection matrix onto the null space of $\mathbf{A}$. Thus, Eq. (41) can be expressed by $\omega_f^T\mathbf{P}_n\boldsymbol{\eta} = P_m$, which after substituting Eq. (42) has the minimum norm solution

$$\boldsymbol{\eta} = \mathbf{P}_n\omega_f(\omega_f^T\mathbf{P}_n\omega_f)^{-1}P_m \tag{43}$$

Finally, the power tracking torque is given by Eq. (44),

$$T_n = \mathbf{P}_n\omega_f(\omega_f^T\mathbf{P}_n\omega_f)^{-1}P_m \tag{44}$$

Magnetic Bearing Suspension System With MIMO (Gyro) Control. In general, a MB suspension system includes position sensors, controllers, filters, power amplifiers, and MB actuators. Figures 4 and 5 show a feedback diagram of a typical magnetic

Downloaded From: http://asmedigitalcollection.asme.org/ on 04/07/2015 Terms of Use: http://asme.org/terms

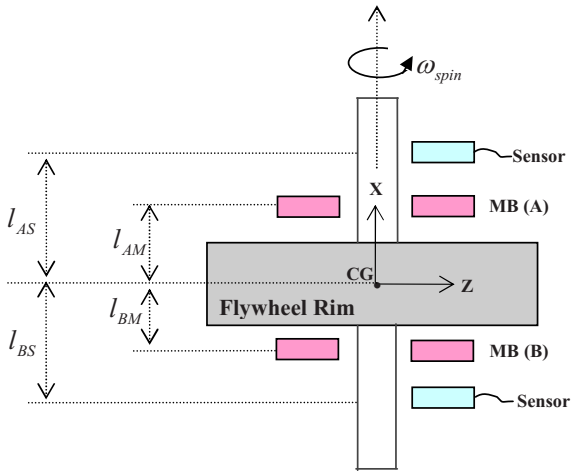

Fig. 5 Flywheel system with a MB suspension

suspension system and a diagram of a flywheel with a MB suspension, respectively.

Position Sensor. Magnetic suspensions typically utilize eddy current, optical or reluctance based sensors. The bandwidths of these devices are typically >5 kHz, so they are treated as ideal, infinite bandwidth devices with sensitivity gain.

Voltage and Displacement Errors at Position Sensor. Figure 6 shows the orthogonal sensor pairs at the *A* and *B* bearings and the conversion of the position errors to voltage errors for input to the controller stage.

The voltage errors are expressed in terms of the position errors as follows:

$$\Delta^V = \begin{Bmatrix} \Delta^V_{YA} \\ \Delta^V_{YB} \\ \Delta^V_{ZA} \\ \Delta^V_{ZB} \end{Bmatrix} = \begin{Bmatrix} V^S_{YA} - V^{S,T}_{YA} \\ V^S_{YB} - V^{S,T}_{YB} \\ V^S_{ZA} - V^{S,T}_{ZA} \\ V^S_{ZB} - V^{S,T}_{ZB} \end{Bmatrix} = \begin{Bmatrix} \zeta^S_{YA} \cdot Y^S_A - \zeta^S_{YA} \cdot Y^{S,T}_A \\ \zeta^S_{YB} \cdot Y^S_B - \zeta^S_{YB} \cdot Y^{S,T}_B \\ \zeta^S_{ZA} \cdot Z^S_A - \zeta^S_{ZA} \cdot Z^{S,T}_A \\ \zeta^S_{ZB} \cdot Z^S_B - \zeta^S_{ZB} \cdot Z^{S,T}_B \end{Bmatrix}$$

$$= \begin{bmatrix} \zeta^S_{YA} & 0 & 0 & 0 \\ 0 & \zeta^S_{YB} & 0 & 0 \\ 0 & 0 & \zeta^S_{ZA} & 0 \\ 0 & 0 & 0 & \zeta^S_{ZB} \end{bmatrix} \begin{Bmatrix} e_{YA} \\ e_{YB} \\ e_{ZA} \\ e_{ZB} \end{Bmatrix} \quad \text{or } \Delta^V = \zeta^S \cdot \bar{e}_S \qquad (45)$$

where

$$\zeta^S = \begin{bmatrix} \zeta^S_{YA} & 0 & 0 & 0 \\ 0 & \zeta^S_{YB} & 0 & 0 \\ 0 & 0 & \zeta^S_{ZA} & 0 \\ 0 & 0 & 0 & \zeta^S_{ZB} \end{bmatrix} \quad \bar{e}_S = \begin{Bmatrix} Y^S_A - Y^{S,T}_A \\ Y^S_B - Y^{S,T}_B \\ Z^S_A - Z^{S,T}_A \\ Z^S_B - Z^{S,T}_B \end{Bmatrix} = \begin{Bmatrix} e_{YA} \\ e_{YB} \\ e_{ZA} \\ e_{ZB} \end{Bmatrix}$$

Motion Coordinate Transformation. Figure 7 provides a diagram to determine the approximate rigid body motion coordinates from the measured coordinates at the sensors. This approach is justified since the flexible modes are typically above 1 kHz.

The approximate rigid body motion coordinates are given by

$$Y = \left(\frac{l_{BS}}{l_{AS} + l_{BS}}\right) Y^S_A + \left(\frac{l_{AS}}{l_{AS} + l_{BS}}\right) Y^S_B$$

$$\theta_Z \cong \frac{Y^S_A - Y}{l_{AS}} = \left(\frac{1}{l_{AS}}\right) Y^S_A - \left(\frac{1}{l_{AS}}\right) Y$$

$$Z = \left(\frac{l_{BS}}{l_{AS} + l_{BS}}\right) Z^S_A + \left(\frac{l_{AS}}{l_{AS} + l_{BS}}\right) Z^S_B,$$

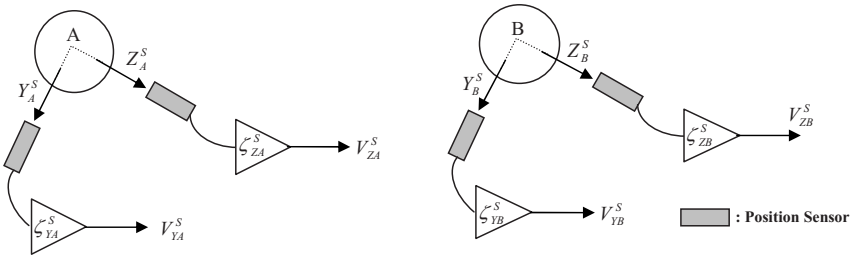

Fig. 6 Position sensor output voltages

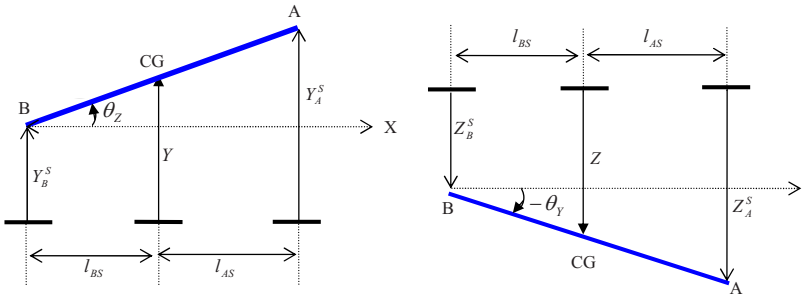

Fig. 7 Motion coordinates transformation

Downloaded From: http://asmedigitalcollection.asme.org/ on 04/07/2015 Terms of Use: http://asme.org/terms

$$\theta_Y \cong -\frac{Z_A^S - Z}{l_{AS}} = -\left(\frac{1}{l_{AS}}\right)Z_A^S + \left(\frac{1}{l_{AS}}\right)Z \tag{46}$$

Errors in the Y, θ_Z and Z, θ_Y coordinates are expressed in terms of the sensor error voltages from Eqs. (45) and (46) as

$$e_Y = Y - Y^T = \gamma_{YA} \cdot \Delta_{YA}^V + \gamma_{YB} \cdot \Delta_{YB}^V$$

$$e_{\theta Z} = \theta_Z - \theta_Z^T = \psi_{\theta Z1} \cdot \Delta_{YA}^V + \psi_{\theta Z2} \cdot e_Y$$

$$e_Z = Z - Z^T = \gamma_{ZA} \cdot \Delta_{ZA}^V + \gamma_{ZB} \cdot \Delta_{ZB}^V$$

$$e_{\theta Y} = \theta_Y - \theta_Y^T = \psi_{\theta Y1} \cdot \Delta_{ZA}^V + \psi_{\theta Y2} \cdot e_Z \tag{47}$$

A matrix form of these equations is given by

$$\bar{e}_{\mathrm{CG}} = \begin{Bmatrix} e_Y \\ e_{\theta Y} \\ e_Z \\ e_{\theta Z} \end{Bmatrix} = \begin{bmatrix} \gamma_{YA} & \gamma_{YB} & 0 & 0 \\ 0 & 0 & \psi_{\theta Y1} + \psi_{\theta Y2} \cdot \gamma_{ZA} & \psi_{\theta Y2} \cdot \gamma_{ZB} \\ 0 & 0 & \gamma_{ZA} & \lambda_{ZB} \\ \psi_{\theta Z1} + \psi_{\theta Z2} \cdot \gamma_{YA} & \psi_{\theta Z2} \cdot \gamma_{YB} & 0 & 0 \end{bmatrix} \begin{Bmatrix} \Delta_{YA}^V \\ \Delta_{YB}^V \\ \Delta_{ZA}^V \\ \Delta_{ZB}^V \end{Bmatrix} \quad \text{or } \bar{e}_{\mathrm{CG}} = T_{\mathrm{DCT}} \cdot \Delta^V \tag{48}$$

where

$$\gamma_{YA} = \frac{l_{BS}}{(l_{AS} + l_{BS})\zeta_{YA}^S}, \quad \gamma_{YB} = \frac{l_{AS}}{(l_{AS} + l_{BS})\zeta_{YB}^S}$$

$$\psi_{\theta Z1} = \frac{1}{l_{AS} \cdot \zeta_{YA}^S} \quad \psi_{\theta Z2} = \frac{-1}{l_{AS}}$$

$$\gamma_{ZA} = \frac{l_{BS}}{(l_{AS} + l_{BS})\zeta_{ZA}^S}, \quad \gamma_{ZB} = \frac{l_{AS}}{(l_{AS} + l_{BS})\zeta_{ZB}^S}$$

$$\psi_{\theta Y1} = \frac{-1}{l_{AS} \cdot \zeta_{ZA}^S}, \quad \psi_{\theta Y2} = \frac{1}{l_{AS}}$$

Power Amplifier. The power amplifier transforms controller output voltages to currents that flow through the MB coils. Pulse width modulated servoamplifiers are commonly used due to low power consumption and accurate tracking of the demanded currents. A simplified feedback model of a servoamplifier including nonlinearities such as voltage and current saturation is shown in Fig. 4. The closed-loop system transfer function of a servopower amplifier may be represented in a simplified form with proportional gain (K_{PA}), feedback gain (χ), coil inductance, and resistance (L, R) as

$$G_{PA}(s) = \frac{K_{PA}}{LS + (R + \chi \cdot K_{PA})} \tag{49}$$

Control Currents. The dynamics (bandwidth) of the servopower amplifier is neglected for the sake of illustration of the IPAC-AMB system vibration control. Therefore, the action of the power amplifiers may be approximated by

$$\bar{i}_{PA} = \begin{bmatrix} i_{YA} \\ i_{YB} \\ i_{ZA} \\ i_{ZB} \end{bmatrix} = \begin{bmatrix} K_{YA}^{PA} & 0 & 0 & 0 \\ 0 & K_{YB}^{PA} & 0 & 0 \\ 0 & 0 & K_{ZA}^{PA} & 0 \\ 0 & 0 & 0 & K_{ZB}^{PA} \end{bmatrix} \begin{Bmatrix} V_{YA} \\ V_{YB} \\ V_{ZA} \\ V_{ZB} \end{Bmatrix}$$

$$\text{or } \bar{i}_{PA} = \bar{K}^{PA} \cdot \bar{V}_{\mathrm{ctrl}} \tag{50}$$

Magnetic Bearing: Actuator. The forces produced by a MB actuator on the spinning flywheel shaft are nonlinear function of currents and shaft's relative position in the actuator clearance space. A MB actuator for satellite application will most likely incorporate permanent magnets to supply a bias field to minimize Ohmic losses. This MB type has flux paths and other features that require a more complex model. Thus, for the sake of the illustration purposes, assume that an electromagnetic biased MB is utilized. Figure 8 shows one axis of this MB actuator including coils and their currents. Equation (51) provides a representative form for this force when produced by an electromagnet biased, opposing pole, heteropolar type MB.

$$F = \frac{1}{4} f_f^2 N^2 \mu_0 A_p \left\{ \frac{i_+^2}{(c - x_c)^2} - \frac{i_-^2}{(c + x_c)^2} \right\} \tag{51}$$

and the standard linearized form for the MB force is

$$F = K_{\mathrm{pos}} x_c + K_{\mathrm{cur}} i_c \tag{52}$$

These linearized MB stiffness (K_{pos} and K_{cur}) are obtained from differentiation of Eq. (52) with respect to x_c and i_c, respectively. In this paper, the following properties are utilized for MB stiffness: N is the number of coil turns (13), μ_o is the permeability of free space (12.56×10^{-7} N/A^2), A_p is the cross section area of the magnetic pole (6.7×10^{-4} m^2), i is the total current (bias plus control), c is the nominal air gap (0.020 in.$=5 \times 10^{-4}$ m), x_c is the rotor displacement from the center of the bearing, f_f is the flux derate factor due to fringing, i_c is the control current, $c - x_c$ is the air gap, K_{pos} is the linearized position stiffness, and K_{cur} is the linearized current stiffness.

The force, position, and current model represented by Eq. (52) applies only for a certain type of MB. The model is included here for the sake of illustration. More complex bearings and bearing models, which include eddy currents, fringing, and leakage effects, are discussed in Ref. [29].

Control Current Forces. Let K_{cur} represents the current stiffness matrix. The MB control forces can then be expressed as

$$\bar{F}_C^{\mathrm{BRG}} = \begin{bmatrix} F_{YA}^C \\ F_{YB}^C \\ F_{ZA}^C \\ F_{ZB}^C \end{bmatrix} = \begin{bmatrix} K_{YA}^i & 0 & 0 & 0 \\ 0 & K_{YB}^i & 0 & 0 \\ 0 & 0 & K_{ZA}^i & 0 \\ 0 & 0 & 0 & K_{ZB}^i \end{bmatrix} \begin{Bmatrix} i_{YA} \\ i_{YB} \\ i_{ZA} \\ i_{ZB} \end{Bmatrix}$$

$$\text{or } \bar{F}_C^{\mathrm{BRG}} = K_{\mathrm{cur}} \cdot i_c = K_{\mathrm{cur}} \cdot \bar{i}_{PA} \tag{53}$$

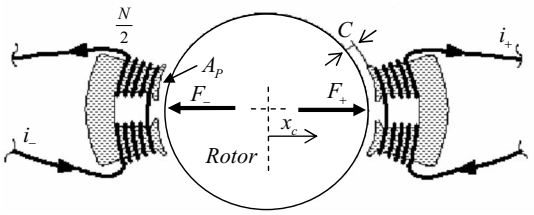

Fig. 8 C-core electromagnet and rotor lamination stack

Downloaded From: http://asmedigitalcollection.asme.org/ on 04/07/2015 Terms of Use: http://asme.org/terms

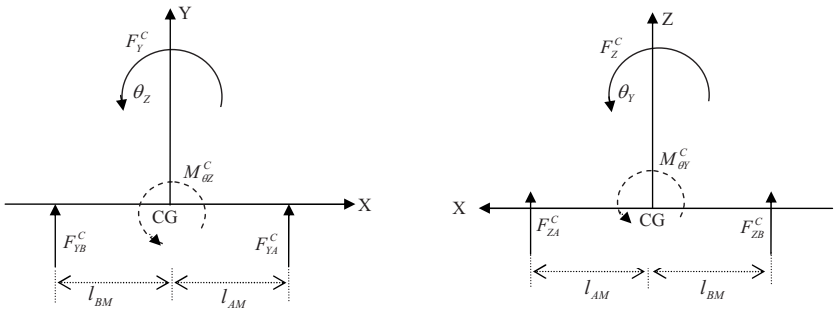

Fig. 9 Force-moment transformation diagram

Transformation Matrix. The coordinate transformation matrix from AMB coordinates to CG (rigid body) coordinates is obtained from Fig. 9 and is given in Eq. (54).

$$\bar{F}_C^{\mathrm{CG}} = \begin{Bmatrix} F_Y^C \\ M_{\theta Y}^C \\ F_Z^C \\ M_{\theta Z}^C \end{Bmatrix} = \begin{bmatrix} 1 & 1 & 0 & 0 \\ 0 & 0 & -l_{AM} & l_{BM} \\ 0 & 0 & 1 & 1 \\ l_{AM} & -l_{BM} & 0 & 0 \end{bmatrix} \begin{Bmatrix} F_{YA}^C \\ F_{YB}^C \\ F_{ZA}^C \\ F_{ZB}^C \end{Bmatrix}$$

$$\text{or } \bar{F}_C^{\mathrm{CG}} = T_{\mathrm{BRG}}^{\mathrm{CG}} \cdot \bar{F}_{\mathrm{C}}^{\mathrm{BRG}} \tag{54}$$

Substitute Eqs. (50) and (53) into, Eq. (54) to obtain the control forces in the CG (rigid body) coordinates

$$\bar{F}_C^{\mathrm{CG}} = T_{\mathrm{BRG}}^{\mathrm{CG}} \cdot \bar{F}_C^{\mathrm{BRG}} = \bar{T}_{\mathrm{BRG}}^{\mathrm{CG}} \cdot K_{\mathrm{cur}} \cdot \bar{K}^{PA} \cdot \bar{V}_{\mathrm{ctrl}} \tag{55}$$

Proportional-Integral-Derivative (PID) Control. Magnetic suspension control laws vary widely according to the particular applications. These include both plant based versions such as H-infinity, QR, sliding mode, etc., or variations of basic PID control. A simple PID type control is described here for the sake of illustration. Filter models are included to represent the natural roll-off of power amplifiers, sensors, and actuators to include effects of antialiasing and smoothing filters and for filter stages intentionally programed into the feedback path for noise rejection. The parallel PID paths are shaped to suppress noise or prevent dc instability and typically have a form similar to

$$G_p(s) = \frac{1}{\tau_p s + 1}, \quad G_I(s) = \frac{1}{\tau_i s + 1}, \quad G_d(s) = \frac{s}{(\tau_d s + 1)^2} \tag{56}$$

For the example presented, the PD controller is implemented with equal time constants τ_p and τ_d, which are selected to make the cutoff frequency $[f_c = 1/2\pi\tau]$ equal to 1024 Hz for both proportional and derivative paths.

Unity Gain PD Transfer Function. The position error terms are differentiated in the controller, yielding a rate feedback variable, as shown in Fig. 10, where

$$T_{\theta Z}(s) = T_Y(s) = T_{\theta Y}(s) = T_Z(s) = \frac{1}{\tau_p s + 1}$$

$$\text{and } T_{\dot{\theta} Z}(s) = T_{\dot{Y}}(s) = T_{\dot{\theta} Y}(s) = T_{\dot{Z}}(s) = \frac{s}{(\tau_d s + 1)^2}$$

PD MIMO Gyro PD Gain Stage. Figure 11 shows the proportional and derivative gain stages and the cross coupling between the tilt directions to form the MIMO, coupled controller.

Figure 11 is represented by the matrix equation

$$\bar{F} = (P_C \cdot e_{\mathrm{CG}}^P + D_C \cdot e_{\mathrm{CG}}^D) \tag{57}$$

where

$$P_C = \begin{bmatrix} G_Y^S/2 & 0 & 0 & 0 \\ 0 & G_{CK\theta}/2 & 0 & G_{\theta Z}^S/2 \\ 0 & 0 & G_Z^S/2 & 0 \\ 0 & G_{\theta Y}^S/2 & 0 & -G_{CK\theta}/2 \end{bmatrix}$$

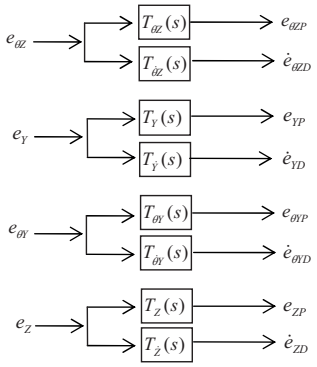

Fig. 10 Unity gain PD transfer function stage

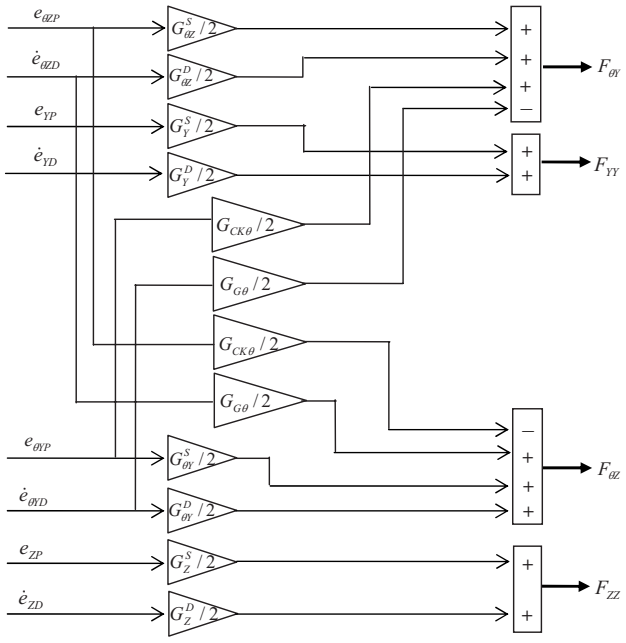

Fig. 11 MIMO-Gyro PD gain diagram

Downloaded From: http://asmedigitalcollection.asme.org/ on 04/07/2015 Terms of Use: http://asme.org/terms

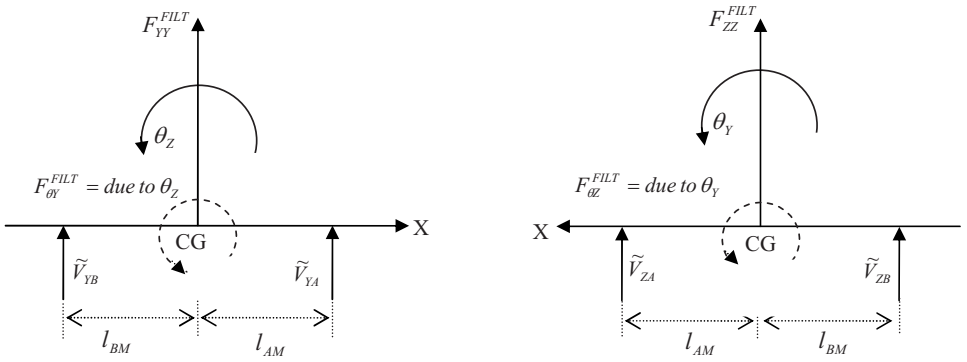

Fig. 12 Diagrams for output coordinate transformation

$$D_C = \begin{bmatrix} G_Y^D/2 & 0 & 0 & 0 \\ 0 & -G_{G\theta}/2 & 0 & G_{\theta Z}^D/2 \\ 0 & 0 & G_Z^D/2 & 0 \\ 0 & G_{\theta Y}^D/2 & 0 & G_{G\theta}/2 \end{bmatrix}$$

$$\bar{F} = \{F_{YY} \quad F_{\theta Y} \quad F_{ZZ} \quad F_{\theta Z}\}^T, \quad e_{\mathrm{CG}}^P = \{e_{YP} \quad e_{\theta YP} \quad e_{ZP} \quad e_{\theta ZP}\}^T$$

$$e_{\mathrm{CG}}^D = \{\dot{e}_{YD} \quad \dot{e}_{\theta YD} \quad \dot{e}_{ZD} \quad \dot{e}_{\theta ZD}\}^T$$

Output Coordinate Transformation Stage. Fig. 12 is diagrams for converting the rigid body coordinate control signals into the two pairs of orthogonal MB actuator coordinates.

Low-pass filter, lead/lag compensation, and notch filter stages are arranged in series at the output end of the controller. A bandpass filter is also utilized to aid in canceling MB forces at the spin frequency due to rotating, mass imbalance. These stages are illustrated in Fig. 4. The outputs of the filter stages are represented by F_{YY}^{Filt}, $F_{\theta Y}^{\mathrm{Filt}}$, F_{ZZ}^{Filt}, and $F_{\theta Z}^{\mathrm{Filt}}$. These quantities are in the rigid body coordinates and must be transformed into the MB actuator coordinates. The transformations are provided in the following equations:

$$\begin{aligned} F_{YY}^{\mathrm{filt}} &= \tilde{V}_{YA} + \tilde{V}_{YB} \\ F_{\theta Y}^{\mathrm{filt}} &= l_{AM} \cdot \tilde{V}_{YA} - l_{BM} \cdot \tilde{V}_{YB} \\ F_{ZZ}^{\mathrm{filt}} &= \tilde{V}_{ZA} + \tilde{V}_{ZB} \\ F_{\theta Z}^{\mathrm{filt}} &= l_{BM} \cdot \tilde{V}_{ZB} - l_{AM} \cdot \tilde{V}_{ZA} \end{aligned} \tag{58}$$

$$\tilde{V} = \begin{Bmatrix} \tilde{V}_{YA} \\ \tilde{V}_{YB} \\ \tilde{V}_{ZA} \\ \tilde{V}_{ZB} \end{Bmatrix} = \frac{1}{l_{AM} + l_{BM}} \begin{bmatrix} l_{BM} & 1 & 0 & 0 \\ l_{AM} & -1 & 0 & 0 \\ 0 & 0 & l_{BM} & -1 \\ 0 & 0 & l_{AM} & 1 \end{bmatrix} \begin{Bmatrix} F_{YY}^{\mathrm{filt}} \\ F_{\theta Y}^{\mathrm{filt}} \\ F_{ZZ}^{\mathrm{filt}} \\ F_{\theta Z}^{\mathrm{filt}} \end{Bmatrix}$$

$$\text{or } \tilde{V} = T_{\mathrm{MFT}} \cdot \bar{F}^{\mathrm{filt}} \tag{59}$$

where

$$T_{\mathrm{MFT}} = \frac{1}{l_{AM} + l_{BM}} \begin{bmatrix} l_{BM} & 1 & 0 & 0 \\ l_{AM} & -1 & 0 & 0 \\ 0 & 0 & l_{BM} & -1 \\ 0 & 0 & l_{AM} & 1 \end{bmatrix} \text{ and } \bar{F}^{\mathrm{filt}} = \begin{Bmatrix} F_{YY}^{\mathrm{filt}} \\ F_{\theta Y}^{\mathrm{filt}} \\ F_{ZZ}^{\mathrm{filt}} \\ F_{\theta Z}^{\mathrm{filt}} \end{Bmatrix} \tag{60}$$

The final output voltages from the controller are obtained by applying gains to compensate for differences in gains that are external to the controller, i.e., the sensors, amplifiers, and MB axes,

$$\begin{aligned} \bar{V}_{\mathrm{ctrl}} &= \begin{bmatrix} \beta_{YA} & 0 & 0 & 0 \\ 0 & \beta_{YB} & 0 & 0 \\ 0 & 0 & \beta_{ZA} & 0 \\ 0 & 0 & 0 & \beta_{ZB} \end{bmatrix} \begin{Bmatrix} \tilde{V}_{YA} \\ \tilde{V}_{YB} \\ \tilde{V}_{ZA} \\ \tilde{V}_{ZB} \end{Bmatrix} \\ &= \bar{\beta}_{\mathrm{out}} \cdot \tilde{V} \quad \text{where } \bar{V}_{\mathrm{ctrl}} = \begin{Bmatrix} V_{YA} \\ V_{YB} \\ V_{ZA} \\ V_{ZB} \end{Bmatrix} \end{aligned} \tag{61}$$

Effective AMB Stiffness, Damping, and Gyro Cancellation Torque Coefficients. Although the AMB model presented here possesses a finite bandwidth, it is instructive to consider an infinite bandwidth approximation in order to identify equivalent stiffness, damping, and gyrotorque coefficients. For this ideal case, the filter output ($\bar{F}^{\mathrm{filt}}$) equals the filter input ($\bar{F}$). Equation (55) becomes

$$\begin{aligned} \bar{F}_C^{\mathrm{CG}} &= T_{\mathrm{BRG}}^{\mathrm{CG}} \cdot \bar{F}_C^{\mathrm{BRG}} = \bar{T}_{\mathrm{BRG}}^{\mathrm{CG}} \cdot K_{\mathrm{cur}} \cdot \bar{K}^{PA} \cdot \bar{V}_{\mathrm{ctrl}} \\ &= \bar{T}_{\mathrm{BRG}}^{\mathrm{CG}} \cdot K_{\mathrm{cur}} \cdot \bar{K}^{PA} \cdot \bar{\beta}_{\mathrm{out}} \cdot T_{\mathrm{MFT}} \cdot \bar{F} \\ &= \bar{T}_{\mathrm{BRG}}^{\mathrm{CG}} \cdot (K_{\mathrm{cur}} \cdot \bar{K}^{PA} \cdot \bar{\beta}_{\mathrm{out}}) \cdot T_{\mathrm{MFT}} \cdot (P_C \cdot e_{\mathrm{CG}}^P + D_C \cdot e_{\mathrm{CG}}^D) \end{aligned} \tag{62}$$

Let

$$K_{\mathrm{cur}} \cdot \bar{K}^{PA} \cdot \bar{\beta}_{\mathrm{out}} = \begin{bmatrix} \lambda_{YA} & 0 & 0 & 0 \\ 0 & \lambda_{YB} & 0 & 0 \\ 0 & 0 & \lambda_{ZA} & 0 \\ 0 & 0 & 0 & \lambda_{ZB} \end{bmatrix} \tag{63}$$

where $\lambda_{YA} = K_{YA}^i \cdot K_{YA}^{PA} \cdot \beta_{YA}$, $\lambda_{YB} = K_{YB}^i \cdot K_{YB}^{PA} \cdot \beta_{YB}$, $\lambda_{ZA} = K_{ZA}^i \cdot K_{ZA}^{PA} \cdot \beta_{ZA}$, and $\lambda_{ZB} = K_{ZB}^i \cdot K_{ZB}^{PA} \cdot \beta_{ZB}$.

Further assume that the power amplifier and current stiffness gains are identical for all axes, so $K_j^i \cdot K_j^{PA}$ can be expressed as $K^i \cdot K^{PA}$, and assume that the β's are tuned to make

$$\lambda_{YA} = \lambda_{YB} = \lambda_{ZA} = \lambda_{ZB} = K^i \cdot K^{PA} \tag{64}$$

The control forces in the CG (rigid body) coordinates become

Downloaded From: http://asmedigitalcollection.asme.org/ on 04/07/2015 Terms of Use: http://asme.org/terms

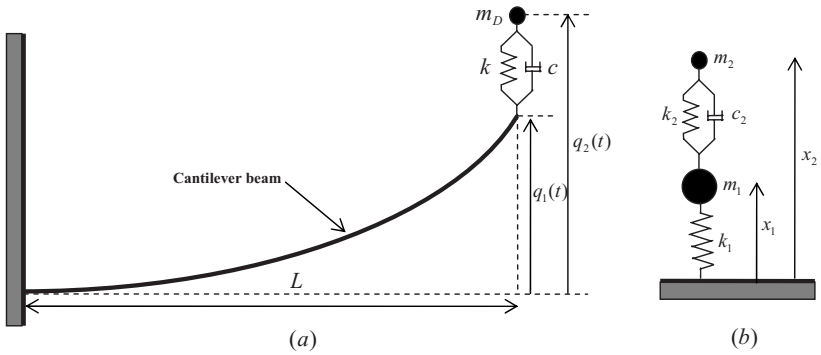

Fig. 13 VCM model

$$\bar{F}_C^{\mathrm{CG}} = \bar{T}_{\mathrm{BRG}}^{\mathrm{CG}} \cdot (K_{\mathrm{cur}} \cdot \bar{K}^{PA} \cdot \bar{\beta}_{\mathrm{out}}) \cdot T_{\mathrm{MFT}} \cdot (P_C \cdot e_{\mathrm{CG}}^P + D_C \cdot e_{\mathrm{CG}}^D)$$

$$= \frac{K^i K^{PA}}{2} \begin{bmatrix} G_Y^S & 0 & 0 & 0 \\ 0 & G_{\theta Y}^S & 0 & -G_{CK\theta} \\ 0 & 0 & G_Z^S & 0 \\ 0 & G_{CK\theta} & 0 & G_{\theta Z}^S \end{bmatrix} \begin{Bmatrix} e_Y \\ e_{\theta Y} \\ e_Z \\ e_{\theta Z} \end{Bmatrix}$$

$$+ \frac{K^i K^{PA}}{2} \begin{bmatrix} G_Y^D & 0 & 0 & 0 \\ 0 & G_{\theta Y}^D & 0 & G_{G\theta} \\ 0 & 0 & G_Z^D & 0 \\ 0 & -G_{G\theta} & 0 & G_{\theta Z}^D \end{bmatrix} \begin{Bmatrix} \dot{e}_Y \\ \dot{e}_{\theta Y} \\ \dot{e}_Z \\ \dot{e}_{\theta Z} \end{Bmatrix} \tag{65}$$

The active stiffness and damping in the CG coordinates are then obtained by comparing Eq. (57) with Eq. (65), yielding

$$F_Y^C = m_f \ddot{e}_Y = \frac{K^i K^{PA}}{2} \{G_Y^S \cdot e_Y + G_Y^D \cdot \dot{e}_Y\} \tag{66}$$

$$M_{\theta Y}^C = I_T \ddot{e}_{\theta Y} + I_P \omega_f \dot{e}_{\theta Z}$$

$$= \frac{K^i K^{PA}}{2} \{G_{\theta Y}^S \cdot e_{\theta Y} - G_{CK\theta} \cdot e_{\theta Z} + G_{\theta Y}^D \cdot \dot{e}_{\theta Y} + G_{G\theta} \cdot \dot{e}_{\theta Z}\} \tag{67}$$

$$F_Z^C = m_f \ddot{e}_Z = \frac{K^i K^{PA}}{2} \{G_Z^S \cdot e_Z + G_Z^D \cdot \dot{e}_Z\} \tag{68}$$

$$M_{\theta Z}^C = I_T \ddot{e}_{\theta Z} - I_P \omega_f \dot{e}_{\theta Y} = \frac{K^i K^{PA}}{2} \{G_{\theta Z}^S \cdot e_{\theta Z} + G_{CK\theta} \cdot e_{\theta Y}$$

$$+ G_{\theta Z}^D \cdot \dot{e}_{\theta Z} - G_{G\theta} \cdot \dot{e}_{\theta Y}\} \tag{69}$$

Therefore, for the ideal, nonsaturated, and infinite bandwidth case, the effective stiffness and damping matrices are as follows:

$$\bar{K}_\infty^{\mathrm{eff}} = \begin{bmatrix} K_{Y,Y} & K_{Y,\theta Y} & K_{Y,Z} & K_{Y,\theta Z} \\ K_{\theta Y,Y} & K_{\theta Y,\theta Y} & K_{\theta Y,Z} & K_{\theta Y,\theta Z} \\ K_{Z,Y} & K & K_{Z,Z} & K_{Z,\theta Z} \\ K_{\theta Z,Y} & K_{\theta Z,\theta Y} & K_{\theta Z,Z} & K_{\theta Z,\theta Z} \end{bmatrix}$$

$$= \frac{K^i K^{PA}}{2} \begin{bmatrix} G_Y^S & 0 & 0 & 0 \\ 0 & G_{\theta Y}^S & 0 & -G_{CK\theta} \\ 0 & 0 & G_Z^S & 0 \\ 0 & G_{CK\theta} & 0 & G_{\theta Z}^S \end{bmatrix} \tag{70}$$

$$\bar{C}_\infty^{\mathrm{eff}} = \begin{bmatrix} C_{Y,Y} & C_{Y,\theta Y} & C_{Y,Z} & C_{Y,\theta Z} \\ C_{\theta Y,Y} & C_{\theta Y,\theta Y} & C_{\theta Y,Z} & C_{\theta Y,\theta Z} \\ C_{Z,Y} & C & C_{Z,Z} & C_{Z,\theta Z} \\ C_{\theta Z,Y} & C_{\theta Z,\theta Y} & C_{\theta Z,Z} & C_{\theta Z,\theta Z} \end{bmatrix}$$

$$= \frac{K^i K^{PA}}{2} \begin{bmatrix} G_Y^D & 0 & 0 & 0 \\ 0 & G_{\theta Y}^D & 0 & G_{G\theta} \\ 0 & 0 & G_Z^D & 0 \\ 0 & -G_{G\theta} & 0 & G_{\theta Z}^D \end{bmatrix} \tag{71}$$

Equations (66)–(69) may be inverted to solve for the required MIMO gains in terms of the required natural frequencies and damping ratios as

$$G_Y^S = \frac{2 m_f \omega_{\mathrm{cyl}}^2}{K^i K^{PA}}, \quad G_Y^D = \frac{4 m_f \zeta_{\mathrm{cyl}} \omega_{\mathrm{cyl}}}{K^i K^{PA}}$$

$$G_{\theta Y}^S = \frac{2 I_T \omega_{\mathrm{con}}^2}{K^i K^{PA}}, \quad G_{\theta Y}^D = \frac{4 I_T \zeta_{\mathrm{con}} \omega_{\mathrm{con}}}{K^i K^{PA}}$$

$$G_Z^S = G_Y^S, \quad G_Z^D = G_Y^D, \quad G_{\theta Z}^S = G_{\theta Y}^S, \tag{72}$$

Table 1 VCM damping ratios versus VCM attachment stiffness and damping

m_D (kg)	c_{opt} (N s/m)	k_{opt} (N/m)	ξ_1	ξ_2	ξ_3	ξ_4	$\xi_{\min}$
0.45	0.9065	10.767	0.1136	0.1136	0.1398	0.1398	0.1136
1.35	6.1197	32.310	0.2757	0.2757	0.2491	0.2491	0.2491
2.25	10.202	39.672	0.3240	0.3240	0.3286	0.3286	0.3240
3.15	14.280	43.575	0.3950	0.3950	0.3878	0.3878	0.3878
4.05	18.370	45.900	0.4888	0.4888	0.43	0.43	0.43

Downloaded From: http://asmedigitalcollection.asme.org/ on 04/07/2015 Terms of Use: http://asme.org/terms

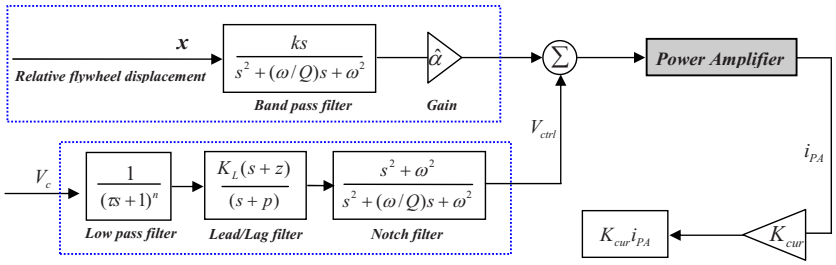

Fig. 14 Filtering employed in the AMB control to attenuate the forces at the spin frequency

$$G^D_{\theta Z} = G^D_{\theta Y}, \quad G_{G\theta} = \frac{2 \cdot I_P \cdot \omega_{\text{spin}}}{K^i K^{PA}} \text{ and } G_{CK\theta} = 0.5 \cdot G^S_{\theta Y}$$

The gyrocontrol gains, $G_{G\theta}$ and $G_{CK\theta}$, are positioned in Eq. (65) to buck (cancel) a portion of the natural gyroscopic moments that result from spinning the flywheel.

Added Masses (VCM) to Control the Vibration of the Satellite's Flexible Appendages. A machine or system may experience excessive vibration if it is acted upon by a force whose excitation frequency nearly coincides with a natural frequency of the machine or system. In such case, the vibration of the machine or system can be reduced by utilizing a dynamic vibration absorber [30]

For the classical vibration absorber case, VCM approach in Fig. 13(*a*) can be modeled as Fig. 13(*b*). The equations of motions, steady-state solutions, and more analytical parts are given by Ref. [30]. The optimum damping ratio can be calculated as $\xi^2_{\text{optimum}} = 3\mu/8(1+\mu)^3$, where $\mu = m_2/m_1$ from Fig. 13(*b*) [30]. In the case of 1.35 kg VCM, the mass ratio $(\mu) = 0.3$ and $\xi_{\text{optimum}} = 0.2236$, which is similar to Table 1. For illustration of VCM approach, assume that a flexible appendage behaves similar to a cantilever beam with deflection pattern $y(x,t) = (x/L)^2 q_1(t)$, where $q_1(t)$ is a generalized coordinate for the beam's deflection. The equations of motion for the VCM in Fig. 13(*a*) and the beam coordinate become

$$\begin{bmatrix} \frac{\rho AL}{5} & 0 \\ 0 & m_D \end{bmatrix} \begin{Bmatrix} \ddot{q}_1 \\ \ddot{q}_2 \end{Bmatrix} + \begin{bmatrix} c & -c \\ -c & c \end{bmatrix} \begin{Bmatrix} \dot{q}_1 \\ \dot{q}_2 \end{Bmatrix} + \begin{bmatrix} \frac{4EI}{L^3} + k & -k \\ -k & k \end{bmatrix} \begin{Bmatrix} q_1 \\ q_2 \end{Bmatrix} = \begin{bmatrix} 0 \\ 0 \end{bmatrix} \quad \text{or } M\ddot{q} + C\dot{q} + Kq = 0 \tag{73}$$

where

$$q = \begin{Bmatrix} q_1 \\ q_2 \end{Bmatrix}, \quad M = \begin{bmatrix} \frac{\rho AL}{5} & 0 \\ 0 & m_D \end{bmatrix}, \quad C = \begin{bmatrix} c & -c \\ -c & c \end{bmatrix}$$

$$K = \begin{bmatrix} \frac{4EI}{L^3} + k & -k \\ -k & k \end{bmatrix}$$

The first order form of this equation can be written as

$$\dot{X} = AX \quad \text{where } A = \begin{bmatrix} 0 & I_2 \\ -M^{-1}K & -M^{-1}C \end{bmatrix} \text{ and } X = \begin{Bmatrix} q \\ \dot{q} \end{Bmatrix} \tag{74}$$

The damping ratios (ξ_i) may then be obtained from the eigenvalues of A as

$$\left\{ \xi_i = \frac{\text{abs}[(\text{real part of eigenvalue})_i]}{\text{abs}[(\text{eigenvalue})_i]}, \; i = 1,2,3,4 \right\} \tag{75}$$

The VCM's attachment stiffness and damping were selected to maximize the first mode's damping ratio as illustrated in Table 1.

Flywheel Unbalance Isolation. Mass imbalance of the flywheel creates a force at its spin frequency, which in turn causes a time varying error in the magnetic suspension position control at the spin frequency. This may be very undesirable since the ensuing vibrations can interfere with the proper operation of onboard, precision instrumentation. This may be rectified by positioning the center frequency of a notch filter at the flywheel spin frequency in the feedback path of the magnetic suspension control. Equation (52) shows that there still exists another component of force at the spin frequency due to the position stiffness and vibration. This force is proportional to the relative vibration of the rotor with respect to the stator, and so the force may be canceled by bandpass filtering this relative vibration at the spin frequency and then multiplying this signal by an appropriate gain to create forces that oppose the position stiffness related forces.

The bandpass filter is modeled as a second-order transfer function, as shown in Fig. 14. In addition, a low-pass filter is utilized in the flywheel motor torque feedback loop to remove high frequency components.

The output of the bandpass filter at the flywheel spin speed (40.000 rpm) is $(Q/\omega)x$, where Q is the bandpass quality factor

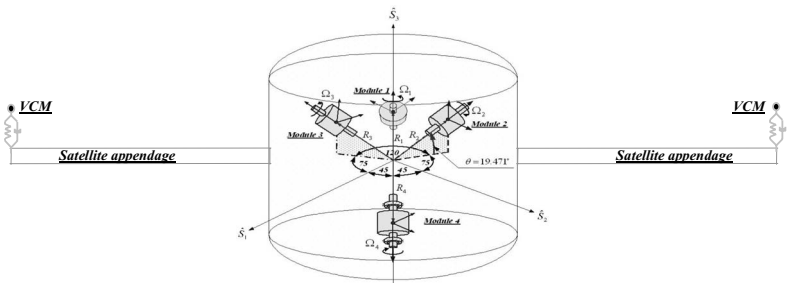

Fig. 15 Tetrahedral array of flywheels attached to the satellite

Downloaded From: http://asmedigitalcollection.asme.org/ on 04/07/2015 Terms of Use: http://asme.org/terms

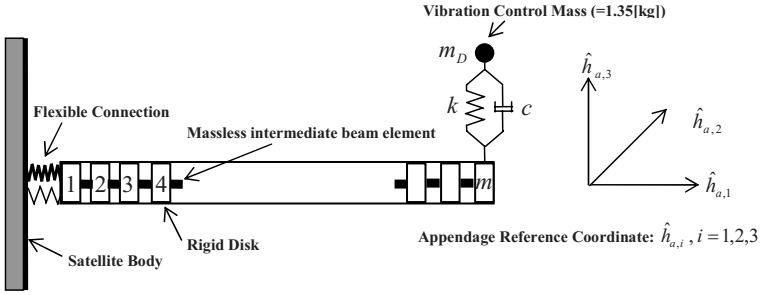

Fig. 16 Flexible appendage model consisting of beam type elements

and x represents the relative vibration (displacement) at the MB actuator location. The total MB force at the spin frequency is expressed as $F_{\mathrm{MB}}=K_{\mathrm{pos}}\cdot x+K_{\mathrm{cur}}\cdot i_{PA}$. The forces applied to the satellite by the MB actuator, at the flywheel spin frequency, will therefore be null if it is assumed that the power amplifier gain is 1 A/V and the gain $\hat{\alpha}$ in Fig. 14 is selected as $\hat{\alpha}=-(K_{\mathrm{pos}}/K_{\mathrm{cur}})\times(\omega/Q)$.

Simulation Results

Model Description. The overall configuration of this example employs four rigid flywheels aligned in a tetrahedral shaped array and two flexible appendages attached to the satellite in Fig. 15 [15]. The mass centers of the flywheels and appendages are offset from the satellite mass center by distances R_i and A_i, respectively. Each flywheel's housing is assumed to be rigid and has a rigid attachment to the satellite. Each appendage's motions are referenced to a fictitious rigid "appendage reference," which coincides with the appendage centerline in the zero motion state, as depicted in Fig. 16. Figure 15 indicates that the flywheel housing body coordinate axes, $\hat{h}_{f,3}$, of Modules 1–3 are separated by 120 deg from each other, and their spin axes make a 19.471 deg angle with respect to the satellite $\hat{S}_1,\hat{S}_2$ plane. Module 4 is perpendicular to this plane and pointed along the $-\hat{S}_3$ axis direction. All flywheel spin directions are in the clockwise sense as viewed from the satellite coordinate origin (Table 2). It is assumed that the satellite inertias include the effects of the flywheel housings and that the

Table 2 Model parameter values Note the following: (1) **: I_a=diag(0.47, 18.4, 18.85 N m s^2) =diag(4.178, 162.7, 167 lb in. s^2), (2) Young's modulus and shear modulus of flexible appendages: $E=2.06\times10^9$ N/m^2 $G=8.27\times10^{10}$ N/m^2, and (3) length of each appendage=3.2 m

Parameters	Weight	$I_P\cdot g$	$I_T\cdot g$	Initial speed	R_f	R_a
Satellite	1360 kg =3000 lb	1693 N m s^2 =15000 lb in. s^2	2258 N m s^2 =20000 lb in. s^2	0		
Flywheel	22.7 kg =50 lb	69.5 N m s^2 =617 lb in. s^2	55.67 N m s^2 =494 lb in. s^2	40,000 rpm	0.61 m =24 in	
Appendage	22.7 kg =50 lb		**	0		2.4 m =95 in

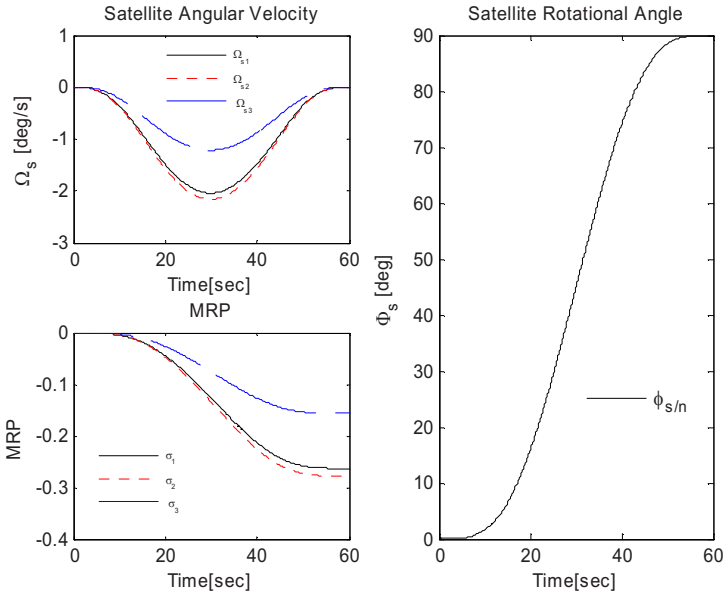

Fig. 17 Satellite reference motion

Downloaded From: http://asmedigitalcollection.asme.org/ on 04/07/2015 Terms of Use: http://asme.org/terms

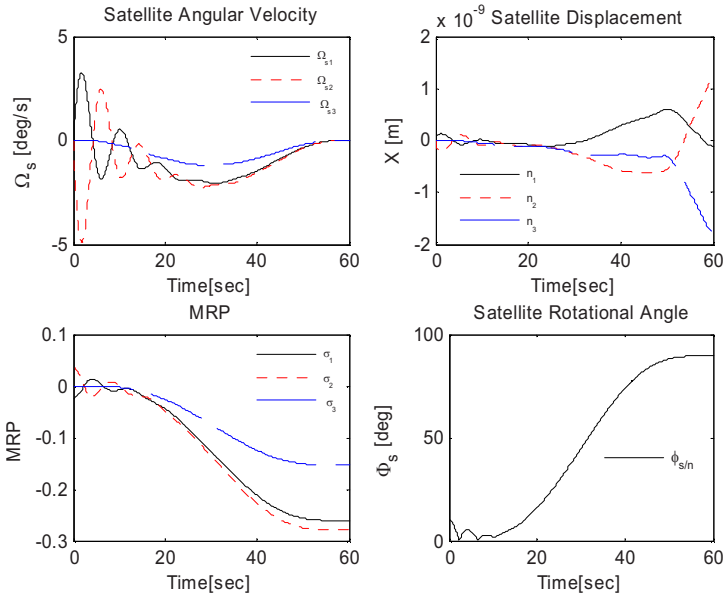

Fig. 18 Satellite motions including flexibility and MB suspension system

MB centers coincide with the flywheel housing centerlines.

The 1.35 kg (3 lb) VCM shown in Fig. 16 is utilized to reduce the vibration of the appendage, thereby reducing ripple error in the power transfer (charge or discharge). This mass is attached to the free end of the appendage utilizing a spring and damper and is constrained in the model to displace only perpendicular to the appendage. The appendage model also includes a small level of structural damping to more closely simulate an actual structure. An actual appendage on a satellite may be collapsible and consists of a trusslike structure with embedded masses and panels. The low stiffness and natural frequencies of this form of appendage are emulated by assigning a low value of Young's modulus for the appendages, which are otherwise modeled as uniform cantilever beams of rectangular cross section.

System Response and IPAC Power Charging and Delivery

Satellite Attitude Maneuver. The reference motion is designed such that the satellite changes orientation 90 deg about EPA of rotation from the initial attitude $[sn]_{ti}$ to the final attitude $[sn]_{tf}$. The EPA is obtained as the eigenvector that corresponds to the eigenvalue +1 of the direction cosine matrix $[\mathbf{C}]$

$$[sn]_{ti} = \begin{bmatrix} 1 & 0 & 0 \\ 0 & 1 & 0 \\ 0 & 0 & 1 \end{bmatrix}, \quad [sn]_{tf} = \begin{bmatrix} 0.3952 & 0.0524 & 0.9170 \\ 0.8037 & 0.4636 & -0.3729 \\ -0.4447 & 0.8844 & 0.1410 \end{bmatrix}$$

$$[\mathbf{C}] = [sn]_{tf}[sn]_{ti}^{T} \quad \text{then the EPA is } l = \begin{pmatrix} 0.6286 \\ 0.6809 \\ 0.3756 \end{pmatrix} \tag{76}$$

$$\text{and the principal angle is } \Phi = \cos^{-1}\left\{\tfrac{1}{2}(C_{11} + C_{22} + C_{33} - 1)\right\} = 90.00 \text{ deg} \tag{77}$$

Generally, the initial actual satellite orientation differs from the reference value. The initial attitude error in this present simulation is assumed to be $[-0.025\ 0.0375\ 0]^T$ in terms of the MRP ($\delta\sigma$), which corresponds to a 10.3 deg principal rotation angle deviation from the reference motion. The reference maneuver rotation is a 90.00 deg EPA change in 60 s, as shown in Fig. 17. Figure 18 shows the satellite's motions with the tetrahedral array of four rigid shaft flywheels, two flexible appendages, and the AMB suspension system (Table 3) for the case of a 10.3 deg initial orientation error. The final rotational angle is 89.99 deg compared to the 90.00 deg target. The satellite's translational motion is negligible and the satellite's angular velocity and orientation errors diminish to zero after about 40 sec, as shown in Fig. 19. The total torque applied to the satellite is shown in Fig. 20.

Comparison of SISO and MIMO AMB Suspension Control. This section compares the robustness of SISO and MIMO control for the case of a $I_P/I_T = 1.25$ flywheel polar to transverse inertia ratio, and PD controller bandwidth of 1024 Hz for both SISO and

Table 3 AMB Parameter Values

Magnetic bearing	Current stiffness K_{cur}	Position stiffness K_{pos}	Load capacity	Locations from flywheel CG
Combo (radial)	41.4 N/A =9.3 lb/A	−1,208,312 N/m =−6,900 lb/in.	444.8 N =100 lb	l_{MB}=0.127 m =5 in.
Combo (axial)	85.5 N/A =19 lb/A	−1,383,448 N/m =−7,900 lb/in.	889.6 N =200 lb	l_{MB}=0.127 m =5 in.
Radial	39.1 N/A =8.8 lb/A	−1,078,739 N/m =−6,160 lb/in.	444.8 N =100 lb	l_{MB}=0.127 m =5 in.

Downloaded From: http://asmedigitalcollection.asme.org/ on 04/07/2015 Terms of Use: http://asme.org/terms

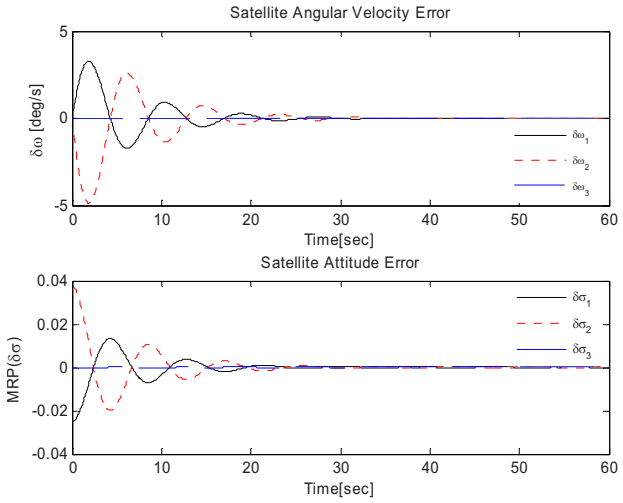

Fig. 19 Satellite error motions

MIMO approaches (Table 4). Saturation states were imposed on the actuator forces at a level of 444.8 N=100 lb, on the voltage applied across the MB coils at 80 V and relative displacement of the flywheel is limited by nominal air gap, which is defined in Eq. (52), (c=0.020 in.=5×10^{-4} m). All attempts to identify stable gains for the decentralized, PD, SISO controller failed, as documented in the figures below. Control requirements to simultaneously reject the initial position error and imbalance disturbances maintain the force and coil voltages in an unsaturated state and provide sufficient gain margin to overcome the controller phase lags that could only be met by the MIMO controller despite many efforts to optimize the SISO controller. The physical reason for this result lies in the MIMO control's ability to cancel the gyroscopic torque that drives the forward and backward conical modes of each flywheel to extremely high or extremely low frequencies, respectively. Figure 21 shows how the relative displacements of the flywheels diverge at each module with SISO control. Figures 23 and 25 show that the corresponding AMB forces and coil voltages oscillate between their + and − saturation values. Figures 22, 24, and 26 show analogous plots for the MIMO control. Stable and unsaturated operations are maintained throughout the satellite model's simulated IPAC operation.

Vibration Control Mass Effects on Flywheels and Flexible Appendages Motions. Each appendage is modeled with five rigid disks connected by flexible Euler–Bernoulli type beam elements. The number of disks is arbitrary and could be easily increased in the model. The proportional damping matrix is employed to stabilize satellite appendage motions. From modal analysis [31], the proportional damping ratio satisfies $2\xi\omega=\alpha+\beta\omega^2$. If α is selected to be zero, the damping ratio can be expressed as $\xi=\beta\omega/2$. It is assumed that the appendage damping ratio increases linearly with frequency, with approximately 5% damping at 2 Hz for the sake of illustration. Figures 27–30 show the flywheel motions and attitude control-power charging torques with and without the VCM. These figures confirm that the "without VCM" oscillations are significantly higher. Power charging responses for the "with and without" VCM cases are shown in Figs. 31 and 32. For illustration, the IPAC operation consists of charging (power transfer) the flywheels at a rate of 500 W for 30 s, while the satellite is simultaneously rotated by 90 deg over a 60 s period. Figures 33 and 34 show the magnified responses of Figs. 31(e) and 32(e), revealing that the power fluctuation is significantly reduced by the VCM. Figures 35 and 36 show the translational motion of the appendage disks relative to the appendage reference line. The disk vibration amplitude increases as one moves along the appendage away from the satellite since the first disk is attached to the satellite with very

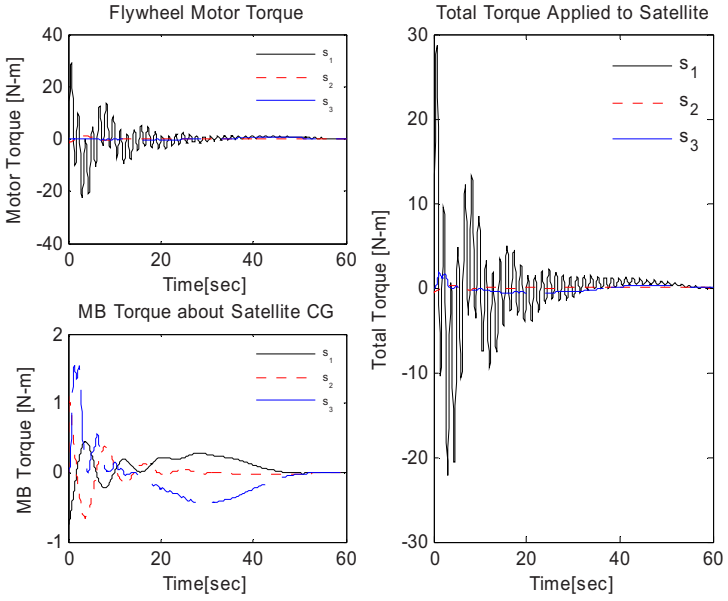

Fig. 20 Torques applied to the satellite

Table 4 AMB and Flywheel Motor Control Gains

MIMO control gains										Motor control gains	
G_Y^S	G_Y^D	$G_{\theta Y}^S$	$G_{\theta Y}^D$	$G_{G\theta}$	G_Z^S	G_Z^D	$G_{\theta Z}^S$	$G_{\theta Z}^D$	$G_{CK\theta}$	k_1	k_2
11.1	0.012	324	0.064	0.67	11.1	0.012	324	0.064	162	15.4	117

Downloaded From: http://asmedigitalcollection.asme.org/ on 04/07/2015 Terms of Use: http://asme.org/terms

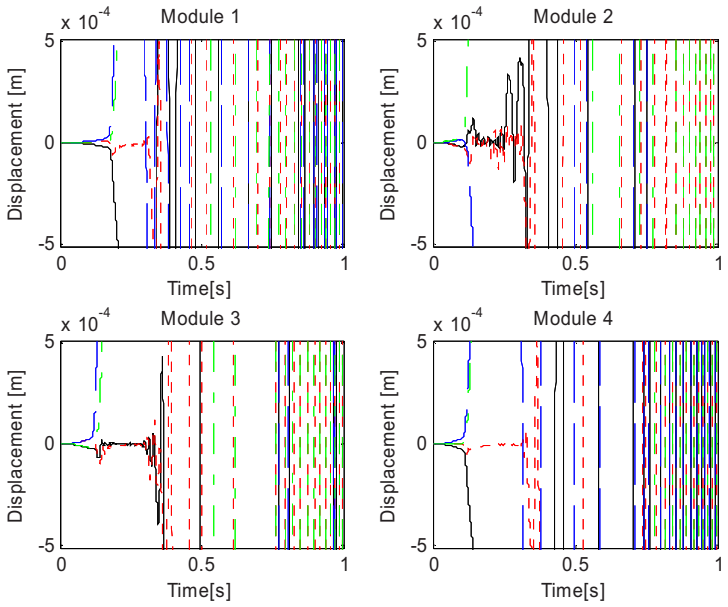

Fig. 21 Displacements of flywheels at sensor position with SISO

stiff linear and torsional springs, so its amplitude is very small. Figure 36 demonstrates the ability of the VCM to reduce appendage vibration.

Figure 37 shows the maximum power ripple and the relative stroke (displacement difference between the VCM and Disk 5) for varying VCM mass with 2% and 5% damping ratios at 2 Hz, respectively. The maximum power ripple is 0.23 W for the case of no VCM; however, this ripple is reduced by about 70% with a (1.35 kg) VCM at 5% damping ratio case. The maximum relative stroke is not significantly affected by increasing the VCM mass.

Isolation of the Satellite From the Flywheel's Mass Imbalance Forces. Figures 38–41 show various of the system responses due to a flywheel imbalance eccentricity of 1×10^{-5} in. ($=2.54\times10^{-7}$ m) at Module 2. Figure 38 shows the AMB forces applied to the satellite and the motor torque without the notch and bandpass filters in the AMB suspension controller and without the low-pass filter in the flywheel motor torque control loop. The maximum forces transmitted to satellite are about 2.8 N and the maximum torques are about 1.25 N m for this case. Figures 39 and 40 show AMB forces and flywheel motor torques with only the notch filter inserted and with both the notch and the bandpass filters inserted, respectively. The transmitted forces and torques are reduced to 0.55 N and 0.258 N m for the notch filter only case, and 0.0035 N and 0.0018 N m for the notch and bandpass filters inserted case, respectively. Figure 41 shows transmitted forces and torques with the low-pass, bandpass, and notch filter (cutoff frequency=100 Hz) systems inserted. The forces are almost the same as Fig. 40; however, the flywheel motor torques are significantly reduced.

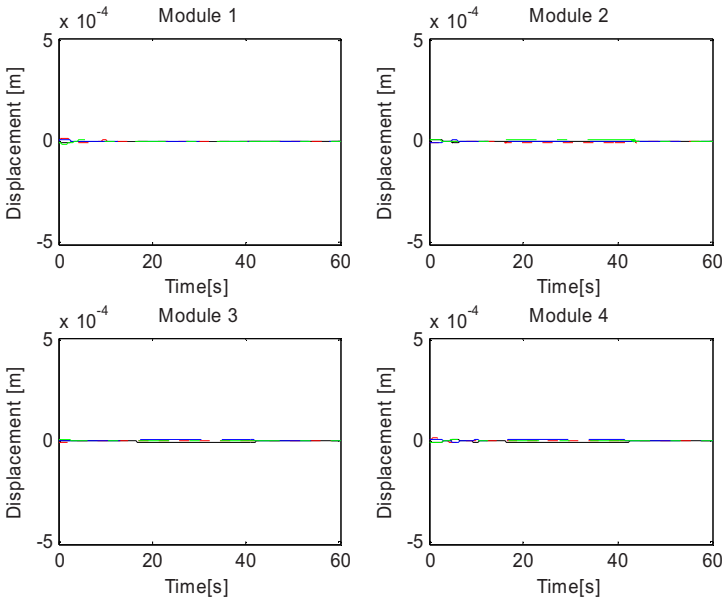

Fig. 22 Displacements of flywheels at sensor position with MIMO

Downloaded From: http://asmedigitalcollection.asme.org/ on 04/07/2015 Terms of Use: http://asme.org/terms

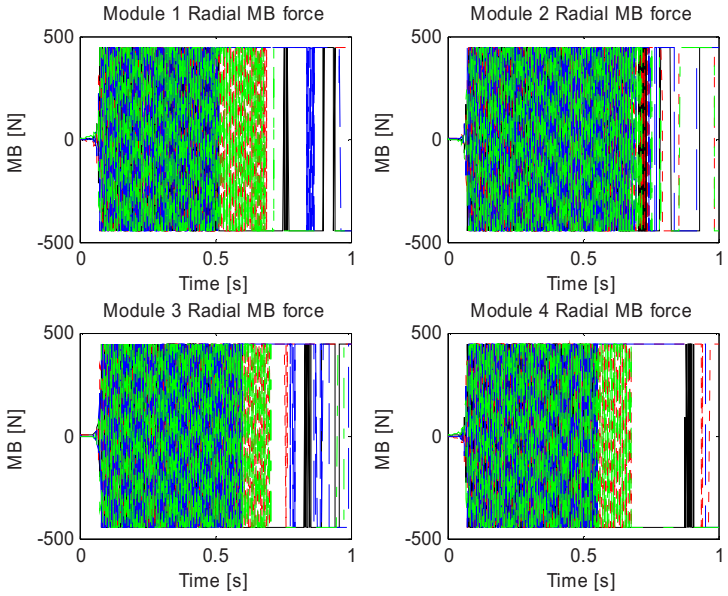

Fig. 23 MB forces at each module (SISO)

Conclusion

A simulated IPAC operation consisting of a 90 deg rotation over 60 s, with a 12% initial attitude error and 500 W power transfer for 30 s was presented. The IPAC algorithm utilized a nonlinear feedback controller and the MBs utilized a special gyrotorque canceling MIMO control. The MB model had a nominal air gap of (5×10^{-4} m, force limit of 444.8 N), and coil voltage limit of 80 V. The VCMs attached to the flexible appendages were very effective for reducing both the power transfer and appendage vibration oscillations. The maximum power ripple is 0.23 W without the VCM at 5% damping ratio, which is reduced by about 70% with a 1.35 kg VCM. The flexible appendage oscillations also nearly disappear after 25 s with the VCM included. The forces transmitted to the satellite were reduced by about 80% by including a notch filter stage in the MIMO control path. In the case when both the notch and bandpass filters were utilized, the transmitted forces were reduced to 3.5×10^{-3} N.

For the example considered, the simulation results confirmed the following objectives:

(1) demonstrate the effectiveness of IPAC with satellite appendage flexibility, and MB feedback dynamics included in the simulation.
(2) demonstrate the effectiveness of passive dampers for suppressing power oscillations in the IPAC system.
(3) demonstrate the effectiveness of a MIMO-Gyro torque canceling AMB control algorithm even for a high I_P/I_T ratio and when coupled with an IPAC model of a satellite.
(4) demonstrate the effectiveness of the MB suspension to isolate the rotor imbalance forces from the satellite body.

Some future work in this area will seek to demonstrate the effectiveness of IPAC as implemented with only two gimbal mounted flywheels including the effects of structural flexibility and MBs.

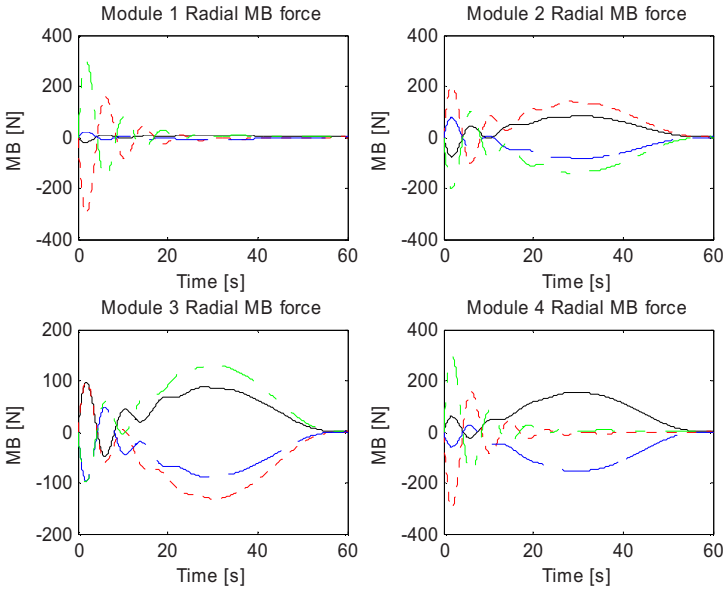

Fig. 24 MB forces at each module (MIMO)

Downloaded From: http://asmedigitalcollection.asme.org/ on 04/07/2015 Terms of Use: http://asme.org/terms

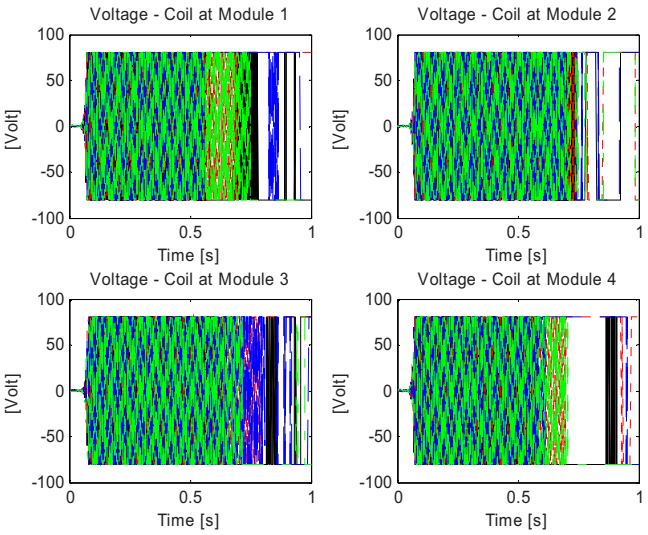

Fig. 25 Coil voltage with SISO

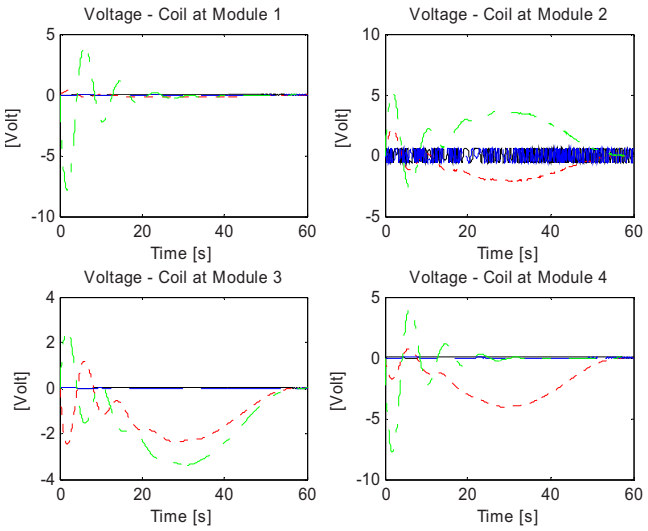

Fig. 26 Coil voltage with MIMO

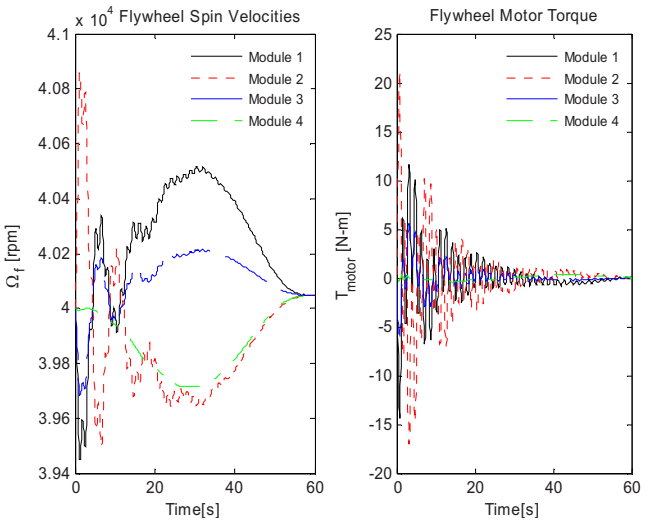

Fig. 27 Flywheel motion without VCM

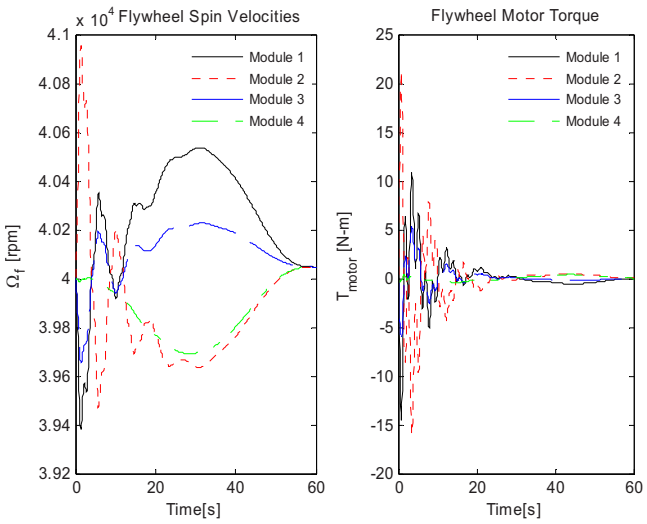

Fig. 28 Flywheel motion with VCM (1.35 kg)

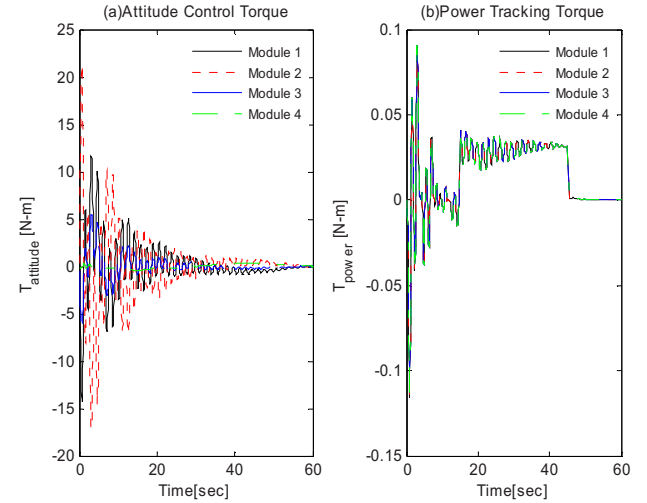

Fig. 29 Attitude control torque and power charging torque without VCM

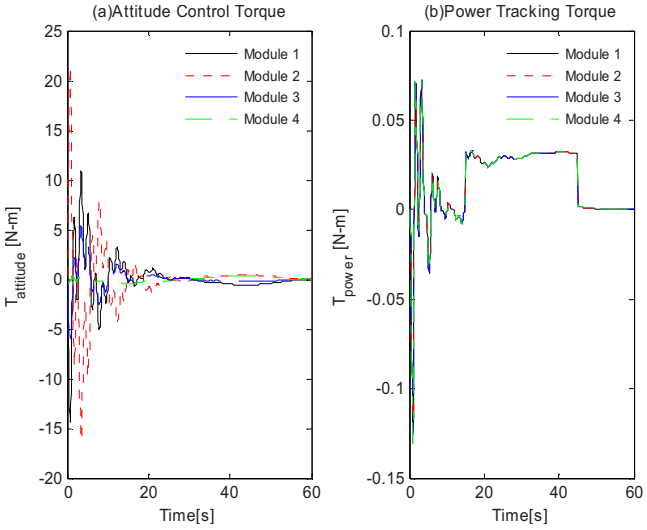

Fig. 30 Attitude control torque and power charging torque with VCM (1.35 kg)

Downloaded From: http://asmedigitalcollection.asme.org/ on 04/07/2015 Terms of Use: http://asme.org/terms

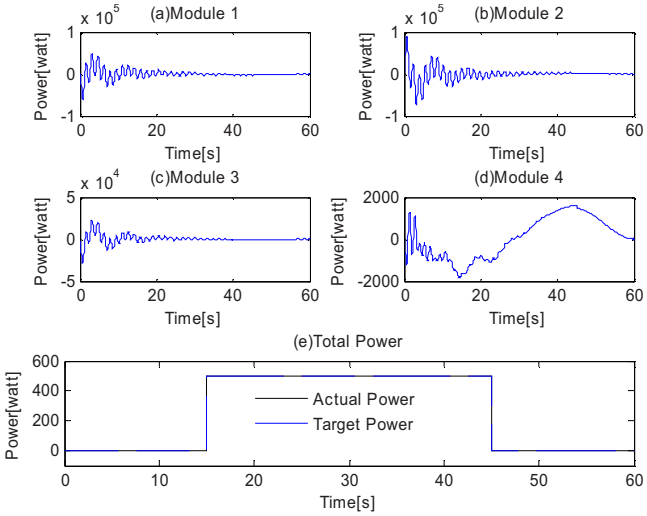

Fig. 31 Power charging response without VCM

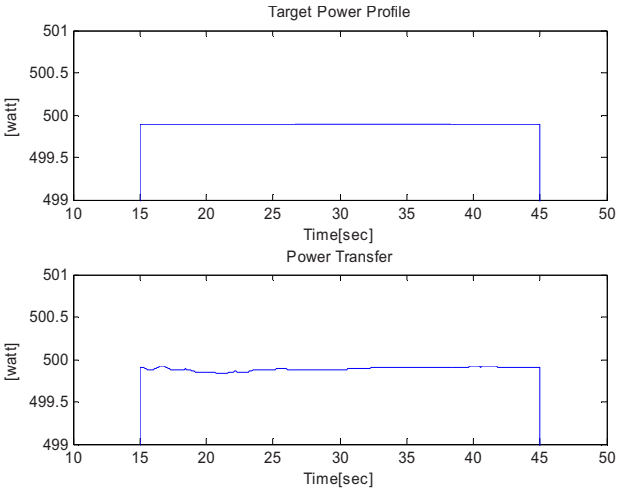

Fig. 34 Power transfer with VCM (1.35 kg)

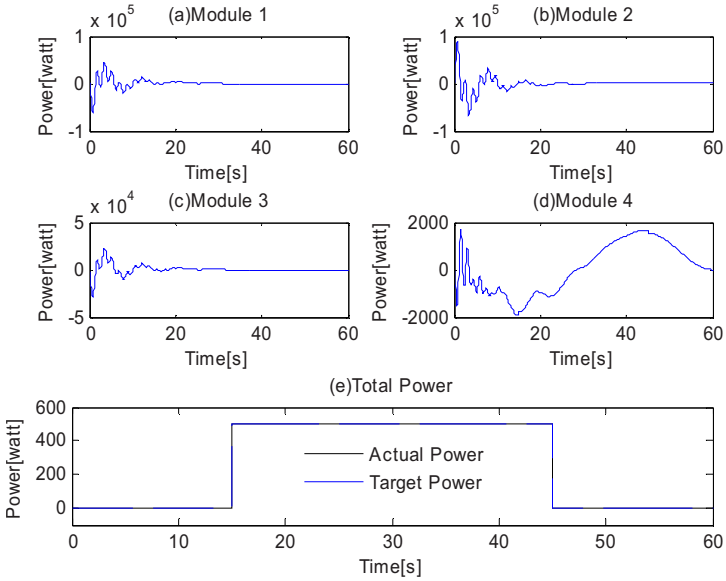

Fig. 32 Power charging response with VCM (1.35 kg)

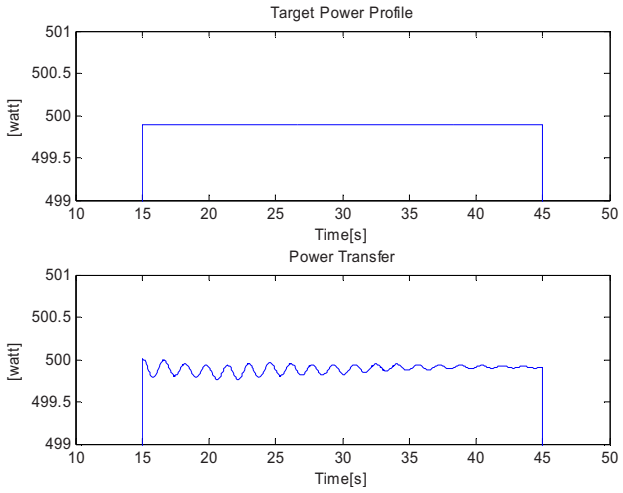

Fig. 33 Power transfer without VCM

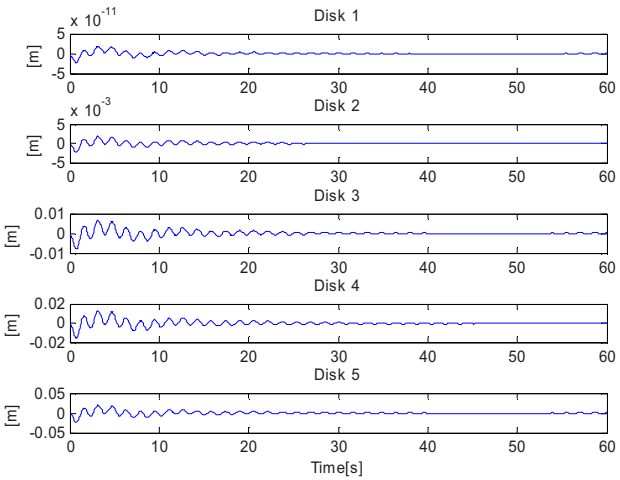

Fig. 35 Vibration along appendage during IPAC without VCM

Downloaded From: http://asmedigitalcollection.asme.org/ on 04/07/2015 Terms of Use: http://asme.org/terms

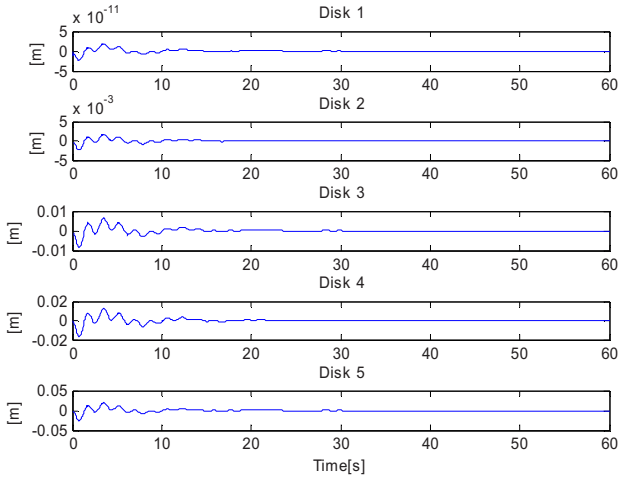

Fig. 36 Vibration along appendage during IPAC with VCM (1.35 kg)

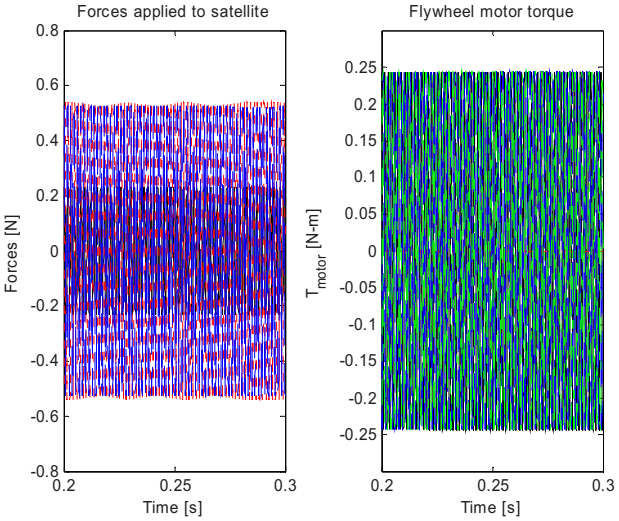

Fig. 39 Forces and motor torques with notch filter

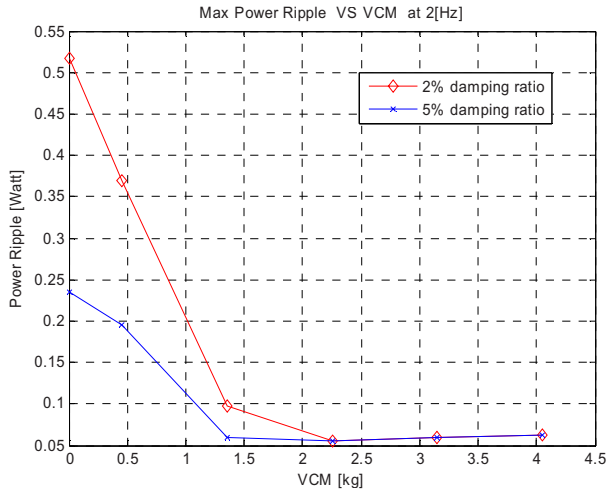

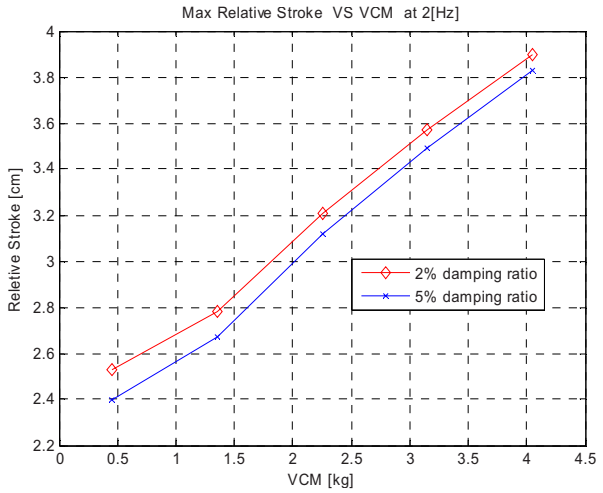

Fig. 37 Maximum power ripple and relative stroke of appendage versus VCM

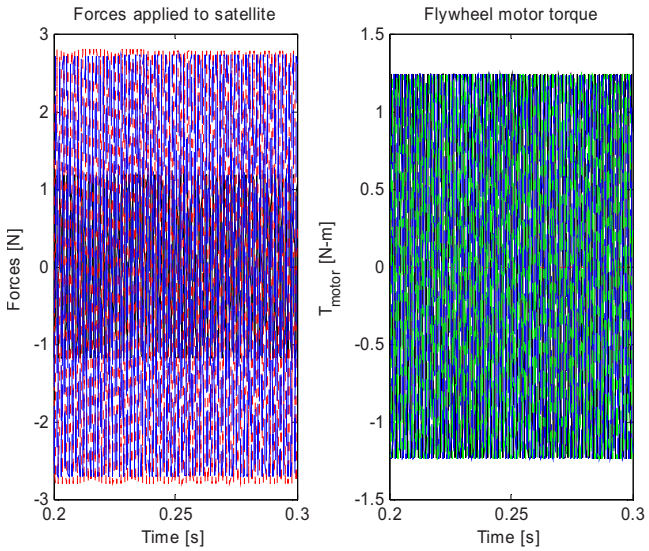

Fig. 38 Forces and motor torques without notch and band-pass filter

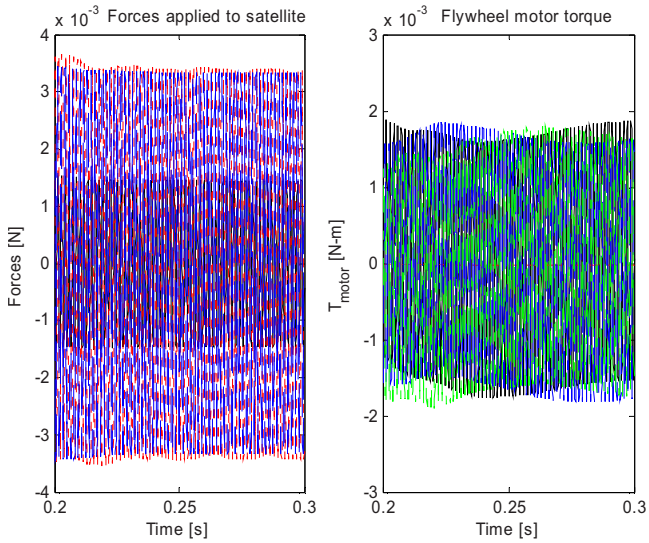

Fig. 40 Forces and motor torques with notch and bandpass filter

Downloaded From: http://asmedigitalcollection.asme.org/ on 04/07/2015 Terms of Use: http://asme.org/terms

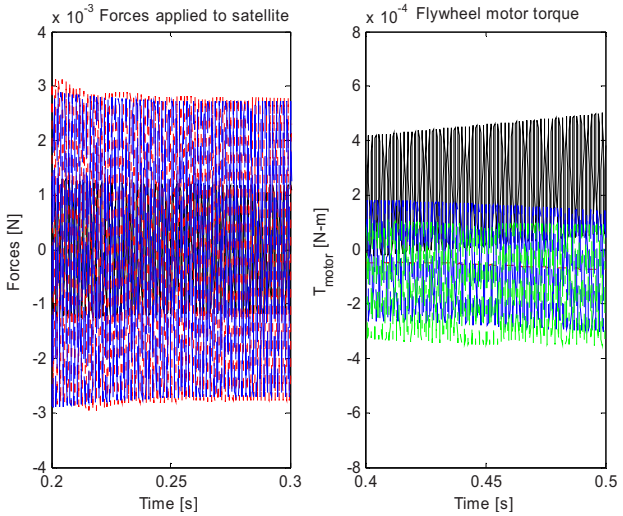

Fig. 41 Forces and motor torques with notch, bandpass, and low-pass filter

Acknowledgment

The authors wish to express their gratitude to the NASA Center for Space Power (CSP) at Texas A&M University and NASA Glenn for funding this research.

Nomenclature

x = displacement of flywheel relative to flywheel housing
y = displacement of appendage relative to appendage reference frame
R_f = offset distance between flywheel housing mass center and satellite CG
R_a = offset distance between flywheel housing mass center and satellite CG
X = displacement of the satellite mass center relative to the inertial frame
m_f = flywheel mass
F_f = MB reaction forces acting on the flywheel
$X^h_{f/s}$ = displacement of flywheel mass center relative to the satellite in the flywheel housing frame
$\dot{X}^h_{f/s}$ = flywheel CG velocity relative to the satellite in the flywheel housing frame
$\dot{X}^h_{f/n}$ = flywheel CG velocity relative to the inertial frame in the flywheel housing frame
$(\dot{x})$ = an overdot with parentheses and subscript denotes the differentiation with respect to time as viewed in the frame indicated by the subscript
M_s = satellite mass including flywheel housings
$[ab]$ = direction cosine matrix between coordinates a and b
Ω_s = satellite angular velocity in the satellite frame
Ω_f = flywheel angular velocity relative to the flywheel housing in the flywheel frame
$\omega_{a/b}$ = angular velocity of a relative to b
I_s = satellite inertia including flywheel housings
I_f = rotational inertia for the flywheel
T_f = torque applied to the flywheel
T_{mt} = flywheel motor torque
T_{MB} = flywheel magnetic bearing torque
m = the number of appendage disks in one appendage finite element model
Σ = the number of flywheel or appendage module. In the work, flywheel module is 4 and appendage is 2
$\Sigma_{j=1}^{m}$ = the number of disks in the each appendage ($m=5$)
ξ = damping ratio
ω = natural frequency
E^e = Young's modulus of beam element
A^e = cross section area of beam element
G^e = elastic shear modulus of beam element
L_e = beam element length of beam element
J^e = torsion constant of beam element
I^e_{xi} = area moment of inertia of beam element
l = Euler's principal axis
t_f = satellite maneuver time (60 s)
α = controls the sharpness of the function f
Δt = αt_f
ω_f = flywheel angular velocity relative to the inertial frame
P = required power
V^S_{YA} = sensor voltage at position A in the Y direction
$V^{S,T}_{YA}$ = target sensor voltage at position A in the Y direction
Y^S_A = displacement of A at sensor position in the Y direction
$Y^{S,T}_A$ = target displacement of A at sensor position in the Y direction
ζ = sensor gain
ω_{cly} = cylindrical mode frequency
ω_{con} = conical mode frequency
ζ_{cly} = cylindrical mode damping ratio
ζ_{con} = conical mode damping ratio
ω_{spin} = flywheel spin frequency

$$\tilde{\omega} \equiv \begin{bmatrix} 0 & -\omega_3 & \omega_2 \\ \omega_3 & 0 & -\omega_1 \\ -\omega_2 & \omega_1 & 0 \end{bmatrix}$$

Appendix

The flywheel's "CG" coordinates include the center of gravity translations (y and z) and the shaft's rigid body rotations (θ_y, θ_z) shown below. The y-z coordinates, referred to in the introduction as "MB" coordinates, are (y_A, z_A, y_B, z_B) as shown in the following figure, and typically refer to the shaft motions at the sensor and/or actuator locations. The following analysis relates the CG and MB coordinates (Fig. 42).

$$\begin{bmatrix} y_A \\ z_A \\ y_B \\ z_B \end{bmatrix} = \begin{bmatrix} 1 & 0 & 0 & l_A \\ 0 & -l_A & 1 & 0 \\ 1 & 0 & 0 & -l_B \\ 0 & l_B & 1 & 0 \end{bmatrix} \begin{bmatrix} y \\ \theta_y \\ z \\ \theta_z \end{bmatrix} \tag{A1}$$

where

$$[y_A \quad z_A \quad y_B \quad z_B]^T = \text{MB coordinate}$$

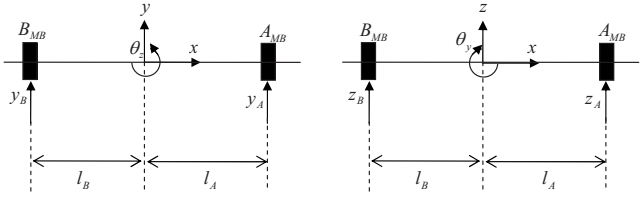

Fig. 42 CG and MB coordinates.

Downloaded From: http://asmedigitalcollection.asme.org/ on 04/07/2015 Terms of Use: http://asme.org/terms

$$[y \quad \theta_y \quad z \quad \theta_z]^T = \text{CG coordinate}$$

References

[1] Tsiotras, P., Shen, H., and Hall, C., 2001, "Satellite Attitude Control for Power Tracking With Energy/Momentum Wheels," J. Guid. Control Dyn., **24**(1), pp. 23–34.

[2] Kim, Y., 2003, "Integrated Power and Attitude Control of a Rigid Satellite With Onboard Magnetic Bearing Suspended Rigid Flywheels," Ph.D. thesis, Texas A&M University, College Station, TX.

[3] Roes, J. B., 1961, "An Electro-Mechanical Energy Storage System for Space Application," *Progress in Astronautics and Rocketry*, Academic, New York, pp. 613–622.

[4] Sindlinger, R., 1976, "Magnetic Bearing Momentum Wheels With Vernier Gimballing Capability for 3 Axis Active Attitude Control and Energy Storage," *Proceedings of the Seventh Symposium on Automatic Control in Space*, Rottach-Egern, West Germany, pp. 849–860.

[5] Brunet, M., 1976, "A New Technology for Three-Axis Stabilized Satellite—Active Magnetic Bearings," *Proceedings of the 27th International Astronautical Federation, International Astronautical Congress*, Anaheim, CA.

[6] Flatley, T. W., 1985, "Tetrahedral Array of Reaction Wheels for Attitude Control and Energy Storage," *Proceedings of the 20th Intersociety Energy Conversion Engineering Conference*, Warrendale, PA, pp. 438–443.

[7] Tsiotras, P., 1994, "New Control Laws for the Attitude Stabilization of Rigid Bodies," *IFAC Symposium on Automatic Control in Aerospace*, Palo Alto, CA, pp. 316–321.

[8] Schaub, H., Robinett, R. D., and Junkins, J. L., 1996, "Global Stable Feedback Laws for Near-Minimum-Fuel and Near-Minimum-Time Pointing Maneuvers for a Landmark—Tracking Spacecraft," J. Astronaut. Sci., **44**(4), pp. 443–466.

[9] Okada, Y., Nagai, B., and Shimane, T., 1992, "Cross Feedback Stabilization of the Digitally Controlled Magnetic Bearing," ASME J. Vibr. Acoust., **114**, pp. 54–59.

[10] Ahrens, M., Traxler, A., Von Burg, P., and Schweitzer, G., 1994, "Design of a Magnetically Suspended Flywheel Energy Storage Device," *Fourth International Symposium on Magnetic Bearing*, ETH Zurich, pp. 553–558.

[11] Na, U., 1999, "Fault-Tolerant Control of Heteropolar Magnetic Bearings," Ph.D. thesis, Texas A&M University, College Station, TX.

[12] Herzog, R., Buhler, P., and Gahler, C., 1996, "Unbalance Compensation Using Generalized Notch Filters in the Multivariable Feedback of Magnetic Bearings," IEEE Trans. Control Syst. Technol., **4**(5), pp. 580–586.

[13] Bhat, P. S., and Bernstein, S. D., 1998, "A Topological Obstruction to Global Asymptotic Stabilization of Rotational Motion and the Unwinding Phenomenon," *Proceedings of the American Control Conference*, Philadelphia, PA, pp. 2785–2789.

[14] Parman, S., and Koguchi, H., 1999, "Controlling the Attitude Maneuvers of Flexible Spacecraft by Using Time-Optimal/Fuel-Efficient Shaped Inputs," J. Sound Vib., **221**(4), pp. 545–565.

[15] Kim, Y., Palazzolo, A., Beach, R., and Provenza, A., 2003, "Interaction Dynamics Between a Satellite and Onboard Magnetically Suspended Flywheels," *First International Energy Conversion Engineering Conference*, Portmouth, VA, Paper No. AIAA 2003-6109.

[16] Ichihara, T., Matsunaga, K., Kita, M., Harabayashi, I., Hirose, M., Yoshi, K., Kurihara, K., Saito, O., Murakami, M., Takabayashi, H., Natsumeda, M., and Koshizuka, N., 2005, "Fabrication and Evaluation of Superconducting Magnetic Bearing for 10 KW H-class Flywheel Energy Storage System," Physica C, **426**(1), pp. 752–758.

[17] Sotelo, G. G., and Ferreira, A. C., 2005, "Halbach Array Superconducting Magnetic Bearing for a Flywheel Energy Storage System," IEEE Trans. Appl. Supercond., **15**(2), pp. 2253–2256.

[18] Sawada, H., Hashimoto, T., and Ninomiya, K., 2001, "High-Stability Attitude Control of Satellite by Magnetic Bearing Wheels," Trans. Jpn. Soc. Aeronaut. Space Sci., **44**(145), pp. 133–141.

[19] Robinson, A. A., 1982, "A Lightweight, Low-Cost, Magnetic-Bearing Reaction Wheel for Satellite Attitude-Control Applications," ESA J. European Space Agency, **6**(4), pp. 397–406.

[20] Jayaraman, C. P., Kirk, J. A., Anand, D. K., and Anjanappa, M., 1991, "Rotor Dynamics of Flywheel Energy Storage Systems," ASME J. Sol. Energy Eng., **113**(1), pp. 11–18.

[21] Kirk, J. A., and Anand, D. K., 1998, "Satellite Power Using a Magnetically Suspended Flywheel Stack," J. Power Sources, **22**(3–4), pp. 301–311.

[22] Kirk, J. A., 1997, "Flywheel Energy—Storage. 1. Basic Concepts," Int. J. Mech. Sci., **19**(4), pp. 223–231.

[23] Kirk, J. A., and Studer, P. A., 1997, "Flywheel Energy—Storage. 2. Magnetically Suspended Super Flywheel," Int. J. Mech. Sci., **19**(4), pp. 223–245.

[24] Kenny, B. H., Kascak, P. E., Jansen, R., Denver, T., and Santiago, T., 2005, "Control of a High-Speed Flywheel System for Energy Storage in Space Applications," IEEE Trans. Ind. Appl., **41**(4), pp. 1029–1038.

[25] Christopher, D. A., and Beach, R., 1998, "Flywheel Technology Development Program for Aerospace Applications," IEEE Aerosp. Electron. Syst. Mag., **13**(6), pp. 9–14.

[26] Junkins, J. L., and Kim, Y., 1993, *Introduction to Dynamics and Control of Flexible Structures* (AIAA Education Series), AIAA, Washington, DC, Chap. 3.5.

[27] Hall, C., Tsiotras, P., and Shen, H., 1998, "Tracking Rigid Body Motion Using Thrusters and Momentum Wheels," AIAA Paper No. AIAA 98-4471.

[28] Tsiotras, P., 1996, "Stabilization and Optimality Results for the Attitude Control Problem," J. Guid. Control Dyn., **19**(4), pp. 772–779.

[29] Meeker, D. C., Maslen, E. H., and Noh, M. D., 1996, "An Augmented Circuit Model for Magnetic Bearings Including Eddy Currents, Fringing, and Leakage," IEEE Trans. Magn., **32**(4), pp. 3219–3227.

[30] Rao, S. S., 1995, *Mechanical Vibrations*, Addison-Wesley, Reading, MA, Chap. 3.6.

[31] Thomson, W. T., 1998, *Theory of Vibration With Applications*, 4th ed., Prentice-Hall, Englewood Cliffs, NJ, pp. 188–189.

Downloaded From: http://asmedigitalcollection.asme.org/ on 04/07/2015 Terms of Use: http://asme.org/terms